Published July 13, 2009

acid) and *N*-methyl-D-aspartate (NMDA)-type glutamate receptors and cell adhesion molecules. The postsynaptic targeting of PSD-95 depends on protein palmitoylation (Topinka and Bredt, 1998). Importantly, palmitate cycling on PSD-95 is dynamically regulated by receptor activation (El-Husseini et al., 2002). Upon glutamate receptor stimulation, accelerated depalmitoylation of PSD-95 dissociates PSD-95 from postsynaptic sites and causes AMPA receptor (AMPAR) endocytosis. This receptor activation–induced depalmitoylation has also been reported in Gα (Wedegaertner and Bourne, 1994). Thus, agonist-dependent depalmitoylation down-regulates synaptic strength and G protein signaling. However, it is not yet clear whether addition of palmitate to proteins is accelerated in response to extracellular signals.

The dynamic regulation of palmitate cycling should be finely tuned by palmitoyl acyltransferases (PATs) and palmitoyl protein thioesterases (PPTs). Transmembrane proteins containing a DHHC (Asp-His-His-Cys) Cys–rich domain (DHHC proteins) have recently emerged as PATs in yeast (Bartels et al., 1999; Lobo et al., 2002; Roth et al., 2002; Linder and Deschenes, 2004). At least 23 mammalian DHHC proteins exist, and a systematic screening method has identified specific enzyme–substrate pairs (Fukata et al., 2004; Fang et al., 2006; Fernandez-Hernando et al., 2006; Fukata et al., 2006; Ponimaskin et al., 2008; Tsutsumi et al., 2009). The DHHC family is present in species ranging from yeast to human and to plants (Hemsley et al., 2005; Hemsley and Grierson, 2008). Several DHHC genes are associated with diseases, including cancers (Oyama et al., 2000), schizophrenia (Mukai et al., 2004, 2008), mental retardation (Mansouri et al., 2005; Raymond et al., 2007), and Huntington's (Yanai et al., 2006). Although the large DHHC family plays essential roles in a range of physiological functions, how the DHHC PAT family is regulated and thereby dynamically controls palmitate cycling remains uncertain.

In this study, we found that suppression of neuronal activity induces palmitoylation and synaptic accumulation of PSD-95. This activity-sensitive PSD-95 palmitoylation recruits synaptic AMPARs. Dendritically localized DHHC2 mediates this rapid synaptic palmitoylation of PSD-95. In contrast, Golgi-resident DHHC3 constitutively palmitoylates PSD-95. These experiments indicate that large DHHC family members are individually regulated, which enables their participation in specific physiological processes such as synaptic plasticity.

Results

Total internal reflection fluorescence microscopy (TIRFM) reveals the synaptic accumulation of PSD-95 upon activity blockade

To follow changes in synaptic PSD-95 accumulation over time, we first performed time-lapse imaging of cultured hippocampal neurons transfected with PSD-95–GFP by TIRFM, which excites only molecules within 100 nm of the cover glass. TIRFM preferentially visualizes wild-type (WT) PSD-95–GFP as discrete punctae on dendrites, which are not seen with cytosolic palmitoylation–deficient (CS) mutant PSD-95 or GFP (Fig. 1, A and B). We confirmed comparable expression levels of PSD-95 (WT) and PSD-95 (CS) in transfected culture (Fig. 1 B). These data confirm that palmitoylation mediates membrane trafficking and synaptic clustering of PSD-95 (Topinka and Bredt, 1998). Because PSD-95 visualized by TIRFM apposes presynaptic synaptophysin and VGLUT1 and overlaps postsynaptic NR1 NMDA receptor (Fig. 1 C), TIRFM tracks synaptic PSD-95. When ionotropic glutamate receptor activity was blocked by kynurenic acid (Kyn), the intensity of PSD-95–GFP by TIRFM steadily increased over 2 h, whereas the intensity of PSD-95 (CS) did not change (Fig. 1, D and E; and Video 1). This Kyn-induced PSD-95 increase was blocked by coapplication of 2-bromopalmitate (2-BP), which is a palmitoyl acyl transfer inhibitor. PSD-95 signals did not detectably change within 2 h of 2-BP treatment alone (Fig. 1 E). These results indicate that newly occurring palmitoylation mediates this synaptic accumulation of PSD-95. Tetrodotoxin (TTX), a blocker of action potentials, also increased PSD-95 accumulation. The dynamic change of PSD-95 intensity was specific to palmitoylation as the localizations of GFP-Rac1-CLLL (Cys-Leu-Leu-Leu), a geranylgeranylated CaaL motif, and synaptophysin-GFP, a presynaptic protein, did not change upon Kyn treatment (Fig. 1 E). Synaptic PSD-95 accumulation upon activity blockade was also confirmed by antibody staining of native PSD-95 (see Fig. 4, C and D). The effect of Kyn or TTX on PSD-95 accumulation does not reflect newly synthesized PSD-95, as cycloheximide (CHX), an inhibitor of protein synthesis, did not affect the Kyn- or TTX-induced PSD-95 increase (Fig. S1, A and B; and Video 2). Thus, PSD-95 palmitoylation increases at the postsynaptic membrane upon activity blockade. These results are complementary to receptor activation–induced depalmitoylation of PSD-95 (El-Husseini et al., 2002).

The DHHC2/15 subfamily of PSD-95 palmitoylating enzymes is regulated by synaptic activity

To monitor PSD-95 palmitoylation biochemically, we used the acyl-biotin exchange (ABE) method (Roth et al., 2006; Kang et al., 2008). We confirmed that this method specifically identified palmitoylated proteins, including PSD-95, in heterologous cells (Fig. S2 A). As previously reported (El-Husseini et al., 2002), treating neurons for 12 h with 2-BP reduced PSD-95 palmitoylation (palmitoylated PSD-95 = 13 ± 15% of control cells; $P < 0.001$; Fig. 2 A). When we treated neurons for 2 h with Kyn, the amount of palmitoylated PSD-95 significantly increased (198 ± 13% of control cells; $P < 0.001$; Fig. 2, A and B). Blocking glutamate receptors with a combination of APV (D-[-]-2-amino-5-phosphonopentanoic acid), which blocks NMDA receptors, and CNQX (6-cyano-7-nitroquinoxaline-2,3-dione), which blocks AMPARs, also enhanced PSD-95 palmitoylation within 2 h (palmitoylated PSD-95 = 184 ± 23% of control cells; $P < 0.01$). 2-BP blocked the rapid enhancement of PSD-95 palmitoylation, indicating that inhibition of depalmitoylation is not solely responsible and that newly occurring palmitoylation mediates this effect. This activity-sensitive PSD-95 palmitoylation is stoichiometric, as Kyn and APV + CNQX quantitatively

Published July 13, 2009

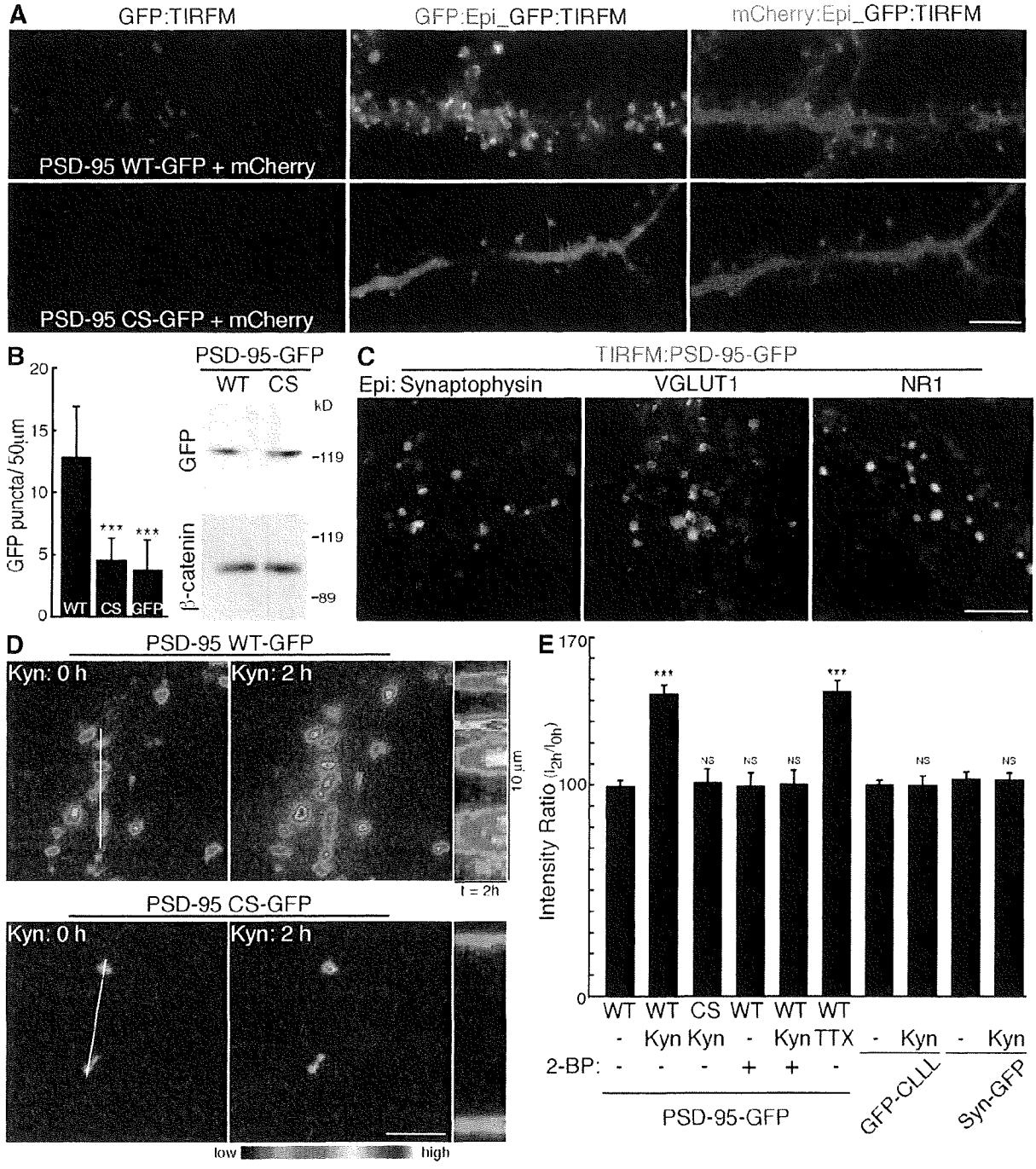

Figure 1. **TIRFM imaging of activity-sensitive PSD-95 palmitoylation.** (A) Compared with epifluorescent microscopy (Epi; green), TIRFM selectively reveals punctae from GFP-tagged PSD-95 (WT) (top; red) but not palmitoylation-deficient PSD-95 (CS) (bottom; red) in cultured hippocampal neurons. To define dendritic morphology, we coexpressed mCherry (Epi; blue). (B) TIRFM preferentially visualizes PSD-95 (WT)–GFP punctae as compared with PSD-95 (CS)–GFP or GFP alone. $n = 10$ neurons; ***, $P < 0.001$. Comparable expression levels of PSD-95 (WT)– and PSD-95 (CS)–GFP in transfected neuron culture were confirmed. (C) TIRFM tracks synaptic PSD-95. PSD-95 punctae (green) visualized by TIRFM apposed presynaptic synaptophysin and VGLUT1 and overlapped postsynaptic NR1. (D) PSD-95–GFP dynamics were analyzed by time-lapse TIRFM imaging. Inhibition of glutamate receptor activity with 10 mM Kyn increased PSD-95 (WT)–GFP intensity within 2 h. In contrast, the palmitoylation-deficient mutant PSD-95 (CS) did not change. Kymographs represent the changes in the intensity of PSD-95–GFP over 2 h. White lines indicate the regions used for the kymographs. (E) Synaptic accumulation of PSD-95 depends on newly occurring palmitoylation. Fluorescent intensities of PSD-95–GFP (WT and CS), GFP containing a C-terminal prenylation CaaL motif of Rac1 (GFP-CLLL), and synaptophysin-GFP (Syn-GFP) at 2 h after the indicated treatments were quantified. The intensity of PSD-95 (WT)–GFP but not other membrane-targeting proteins significantly increased upon 10 mM Kyn or 2 μM TTX treatment. Coapplication of 100 μM 2-BP with Kyn completely inhibited Kyn-induced increase of PSD-95–GFP intensity. $n = 3$–8 experiments; ***, $P < 0.001$ compared with control. (B and E) Error bars indicate SD. Bars: (A) 10 μm; (C and D) 5 μm.

Published July 13, 2009

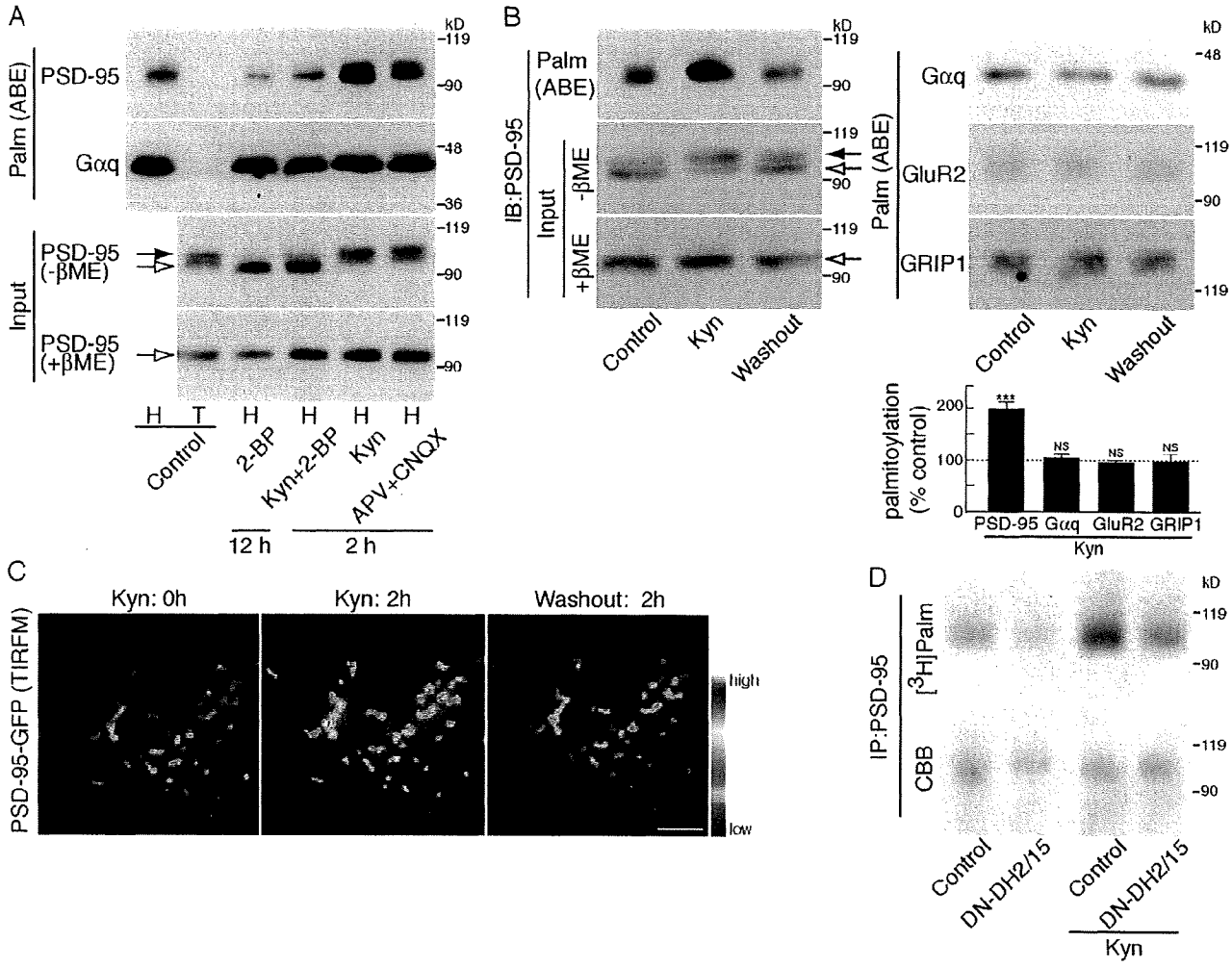

Figure 2. **The DHHC2/15 subfamily of PSD-95 PATs is regulated by synaptic activity.** (A) Activity blockade induces quantitative palmitoylation of PSD-95 but not Gαq. Hydroxylamine (H)-sensitive palmitoylated proteins were purified from treated neurons by the ABE method. The amount of palmitoylated PSD-95 and Gαq was analyzed by Western blotting. T, Tris treatment as a control of hydroxylamine. (B and C) Kyn-induced PSD-95 palmitoylation and synaptic accumulation were reversible upon washing out Kyn. (B) Treatment of hippocampal neurons with Kyn for 2 h enhanced PSD-95 palmitoylation. After washout, PSD-95 palmitoylation level returned to the basal level within 2 h (ABE), with consistent mobility change of PSD-95 (−βME). In contrast, Gαq, GluR2, and GRIP1 palmitoylation did not change upon activity blockade. Kyn-induced palmitoylation changes were quantified. $n = 3$ each; ***, $P < 0.001$. Error bars indicate SD. The dashed line (100%) indicates the normalized control level. IB, immunoblot. (A and B) Closed and open arrows indicate the positions of palmitoylated and nonpalmitoylated PSD-95, respectively. (C) The increased accumulation of PSD-95–GFP upon Kyn treatment returned to the basal level at 2 h after Kyn washout. (D) Cultured hippocampal neurons expressing a DN mutant of the DHHC2 and -15 subfamily (DN-DH2/15) were treated with 3 mCi/ml [^{3}H]palmitate for 2 h in the presence or absence of Kyn. Immunoprecipitated PSD-95 was resolved by SDS-PAGE, followed by fluorography ([^{3}H]palm) and Coomassie staining (CBB). Inhibition of glutamate receptor activity with Kyn greatly enhanced PSD-95 palmitoylation. This enhancement was decreased by DN-DH2/15. IP, immunoprecipitation. Bar, 5 μm.

shifted the PSD-95 band upward (Fig. 2, A and B; Fig. S1 C; and Fig. S2 B). This upward shift reflects palmitoylation, as β-mercaptoethanol (βME), which hydrolyses the palmitoyl thioester, leaves only the lower band (Fig. 2, A and B, bottom). Both the increased PSD-95 palmitoylation and synaptic accumulation were reversible upon washing out of Kyn, indicating that this process is activity sensitive (Fig. 2, B and C).

This activity-sensitive palmitoylation is specific for PSD-95, as Gαq, GluR2, and GRIP1 palmitoylation did not change upon activity blockade (Fig. 2, A and B). Our previous study demonstrated that PSD-95 PATs are DHHC2, -3, -7, and -15, which are phylogenetically divided into two subfamilies, DHHC3/7 and DHHC2/15 (Fukata et al., 2004). Gαq PATs are DHHC3 and -7 (Tsutsumi et al., 2009), and GluR2 PAT is DHHC3 (Fig. S2 C; Hayashi et al., 2005). These substrate selectivities allowed us to ask whether synaptic activity regulates a specific PAT subfamily (i.e., DHHC2/15). We metabolically labeled hippocampal neurons with [^{3}H]palmitic acid for 2 h in the presence or absence of Kyn. We found that Kyn-enhanced PSD-95 palmitoylation was partially blocked by a dominant-negative (DN) mutant, DN-DH2/15, which specifically inhibits the DHHC2/15 subfamily (palmitoylated PSD-95 = 61 ± 15% of Kyn-treated control cells; $P < 0.01$; Fig. 2 D; Fukata et al., 2004). The partial effect of DN-DH2/15 is probably caused by the infection efficiency of DN-DH2/15. Under our conditions, ~50% of neurons were expressing DN-DH2/15,

Published July 13, 2009

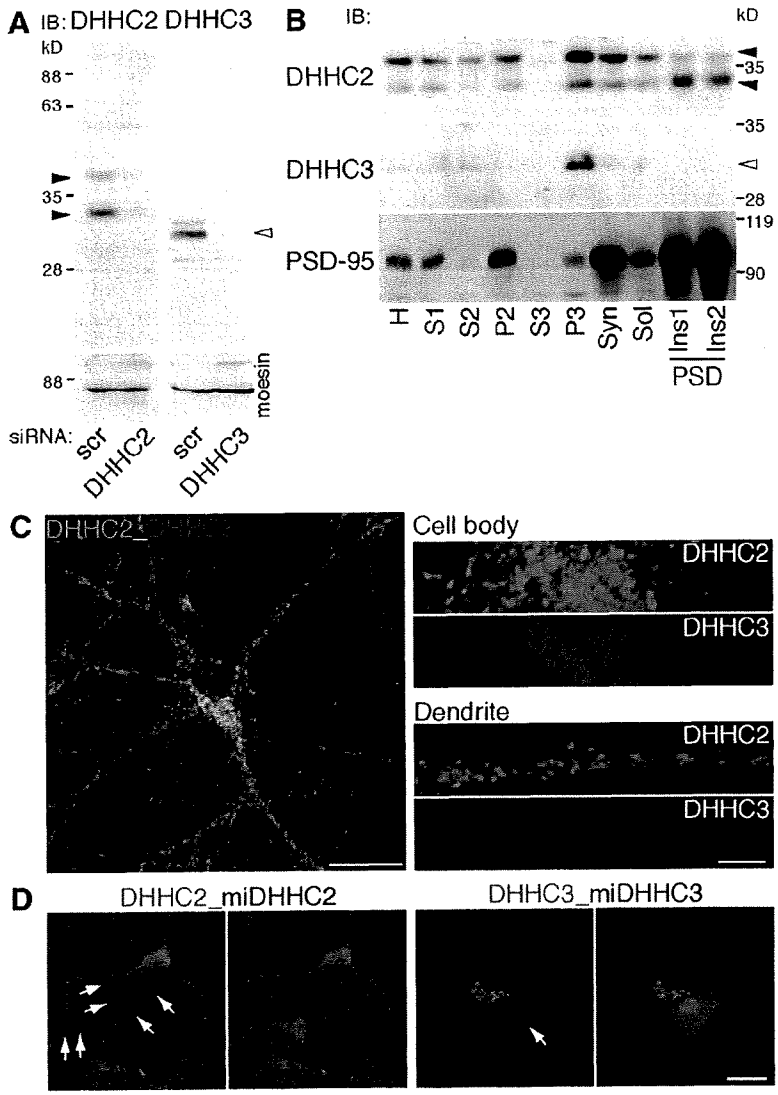

Figure 3. **Differential subcellular distribution of PSD-95 palmitoylating enzymes.** (A) Specificity of antibodies to DHHC2 and -3. The bands detected by anti-DHHC2 (closed arrowheads) and anti-DHHC3 (open arrowhead) antibodies disappeared when protein expression was knocked down by siRNAs. IB, immunoblot; scr, scramble. (B) DHHC2 was enriched in the postsynaptic density (PSD) fractions (Triton X-100–insoluble postsynaptic; closed arrowheads), whereas DHHC3 was detected in only the P3 fraction (open arrowhead). H, homogenate; S, supernatant; P, precipitate; Syn, synaptosome; Sol, Triton X-100 soluble; Ins, Triton X-100–insoluble postsynaptic density fractions. (C) DHHC2 localized in dendrites and the cell body as small vesicular structures, whereas DHHC3 specifically localized at the Golgi apparatus in 18-DIV hippocampal neurons. (D) Effective knockdown of endogenous DHHC2 and -3. Cultured hippocampal neurons were transfected with mCherry-miR RNAi (miDHHC2 and -3) expression vectors at 10 DIV. 18-DIV neurons were stained by DHHC2 or -3 antibody. Note that somatodendritic DHHC2 vesicles and Golgi DHHC3 (arrows) were not stained in mCherry-expressing knocked down neurons (red). Bars: (C [left] and D) 20 µm; (C [right]) 5 µm.

which correlates with the extent of inhibition (~40% inhibition). Although the involvement of other PATs cannot be completely ruled out, our results strongly suggest that the DHHC2/15 subfamily plays a major role in activity-sensitive PSD-95 palmitoylation.

Differential regulation of PSD-95 palmitoylating enzymes in neurons

We next examined the cellular locus for PSD-95 palmitoylation. We focused on DHHC2 and -3, as hippocampal neurons express these PATs but much less DHHC7 and -15 (Fig. S3 A). Immunoblotting with specific antibodies (Fig. 3 A) showed that DHHC2 occurred in the postsynaptic density fraction, whereas DHHC3 was present only in the P3 fraction, which contains Golgi proteins (Fig. 3 B). Consistent with this finding, DHHC3 specifically localizes to the somatic Golgi apparatus (Keller et al., 2004; Tsutsumi et al., 2009), whereas DHHC2 distributes in the dendrites and cell body as small vesicular-like structures (Fig. 3 C). These signals are specific, as the staining completely disappeared in the validated knockdown vector–transfected neuron (Fig. 3 D).

DHHC2 or -3 knockdown by microRNA (miRNA; miDHHCs) greatly reduced the number of PSD-95 punctae (Fig. 4, A and B). Importantly, knockdown of DHHC2 but not DHHC3 prevented Kyn- or TTX-induced increase of endogenous PSD-95 accumulation at synaptic sites (Fig. 4, A, C and D) and Kyn-induced augmentation of PSD-95–GFP accumulation (Fig. 5 and Video 3). The inhibitory effect of miDHHC2 was rescued by miDHHC2-resistant WT DHHC2 (WT) but not by PAT-inactive DHHC2 (CS) (Fig. 5 and Fig. S4 C). These results indicate that DHHC3 localizes to the Golgi apparatus and mediates constitutive palmitoylation of various substrates, including PSD-95, Gαq, and $GABA_A$ receptor-γ subunit (Fukata et al., 2004; Keller et al., 2004; Tsutsumi et al., 2009). In contrast, dendritic DHHC2 mediates activity-sensitive PSD-95 palmitoylation.

Dendritic DHHC2 translocates near postsynaptic sites upon activity blockade

We next investigated whether DHHC2 PAT activity, monitored by autopalmitoylation (Fukata et al., 2004), was regulated by synaptic activity. Whereas PSD-95 palmitoylation increased

Published July 13, 2009

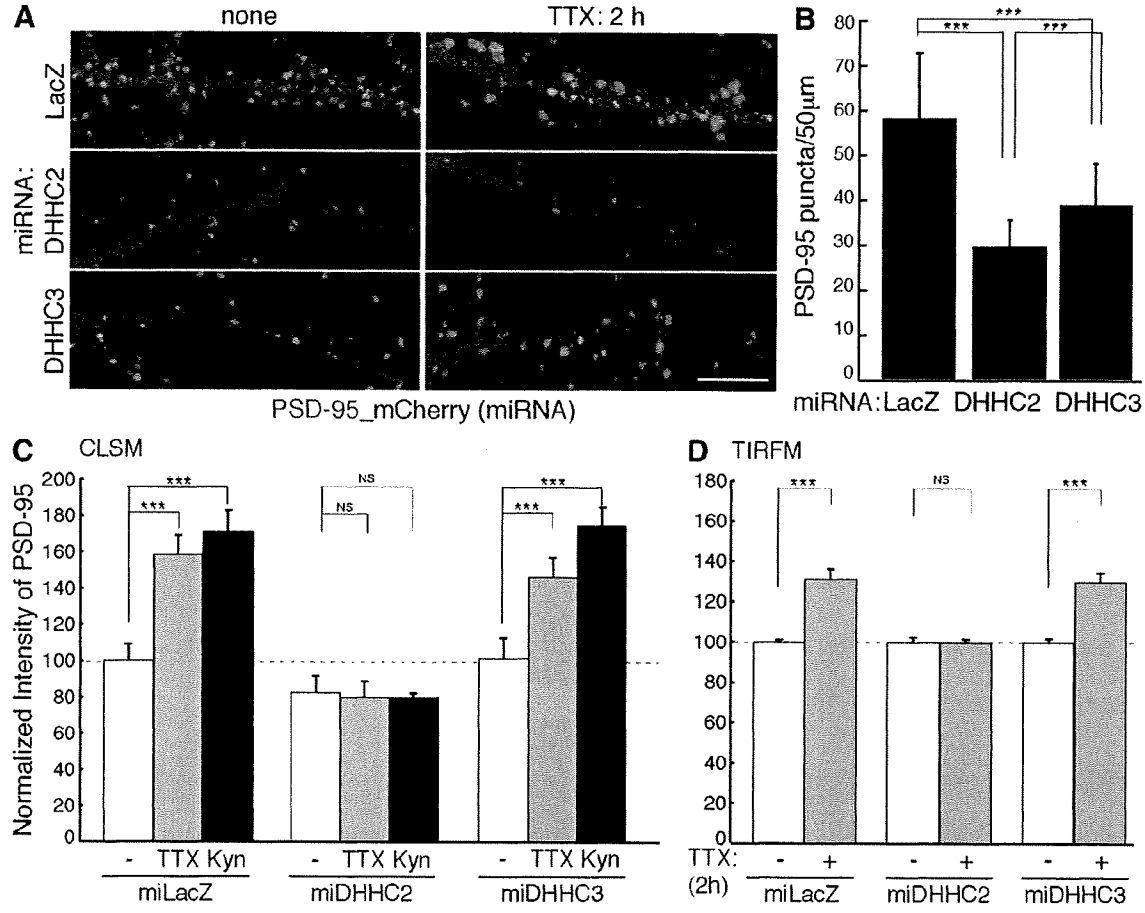

Figure 4. **DHHC2 and -3 are differently involved in PSD-95 trafficking.** (A and B) In the DHHC2 or -3 knocked down neurons (labeled with mCherry), the number of native PSD-95 puncta (green) was significantly decreased. $n = 5$ neurons; ***, $P < 0.001$. (C and D) Knockdown of DHHC2 but not DHHC3 prevented TTX- or Kyn-induced augmentation of endogenous PSD-95 accumulation. Dashed lines (100%) indicate the normalized control level. ***, $P < 0.001$. (C) Analyzed by confocal laser-scanning microscopy (CLSM). $n = 10$–15 neurons. (D) Analyzed by TIRFM. $n = 5$ neurons. miLacZ is a control miRNA targeting LacZ (β-galactosidase). (B–D) Error bars indicate SD. Bar, 5 µm.

upon TTX or Kyn treatment, autopalmitoylation of DHHC2 and -3 did not change (Fig. 6 A), suggesting that DHHC2 activity may remain constant. We then investigated whether DHHC2 localization is regulated by synaptic activity. TIRFM imaging revealed that more DHHC2 was recruited near the membrane upon Kyn or TTX treatment (Fig. 6, B and C; and Video 4), where PSD-95 localized (Fig. S4 A). This translocation was activity sensitive as it was reversible upon washing out of Kyn (Fig. 6 D). Furthermore, we found that Kyn or TTX steadily induced colocalization of endogenous DHHC2 with PSD-95 over 48 h (Fig. 6, E and F), whereas DHHC3 remained at the Golgi apparatus (Fig. S4 B).

Activity-sensitive PSD-95 palmitoylation by DHHC2 is necessary for homeostatic increase of AMPARs

Because PSD-95 anchors AMPARs at the postsynaptic sites through interaction with stargazin and related transmembrane AMPAR regulatory proteins (TARPs; Chen et al., 2000; Nicoll et al., 2006), we investigated changes in synaptic AMPARs upon activity blockade. We took advantage of the pHluorin-tagged GluR1 (pH-GluR1) subunit (Ashby et al., 2004; Yudowski et al., 2007) and TIRFM imaging to monitor specifically surface-expressed GluR1 (Video 5). pH-GluR1 punctate intensity was invariant over 12 h (Fig. 7, A and D; and Video 6). In contrast, TTX treatment gradually and continually increased pH-GluR1 intensity (Fig. 7, B and D; and Video 7). By post hoc immunostaining with PSD-95, we found that pH-GluR1 punctae by TIRFM completely overlapped PSD-95 clusters (Fig. 7 C). Furthermore, knockdown of DHHC2 or PSD-95 completely blocked this increase of pH-GluR1 intensity (Fig. 7, D and E). The effect of DHHC2 knockdown was rescued by miDHHC2-resistant WT DHHC2 (WT) but not by PAT-inactive DHHC2 (CS) (Fig. 7 E and Video 8). The effect of PSD-95 knockdown was rescued by short hairpin RNA–resistant WT PSD-95 (WT) but not by palmitoylation-deficient PSD-95 (CS) (Fig. 7 E, Fig. S4 D, and Video 9). We also found that knockdown of DHHC2 or PSD-95 similarly inhibited Kyn-induced increase of pH-GluR1 (Fig. 7 D). pH-GluR2, endogenous GluR1, GluR2, and stargazin-like TARPs but neither NR2A NMDA receptor nor VGLUT1 showed an increase similar to that of pH-GluR1 (Fig. S5).

Published July 13, 2009

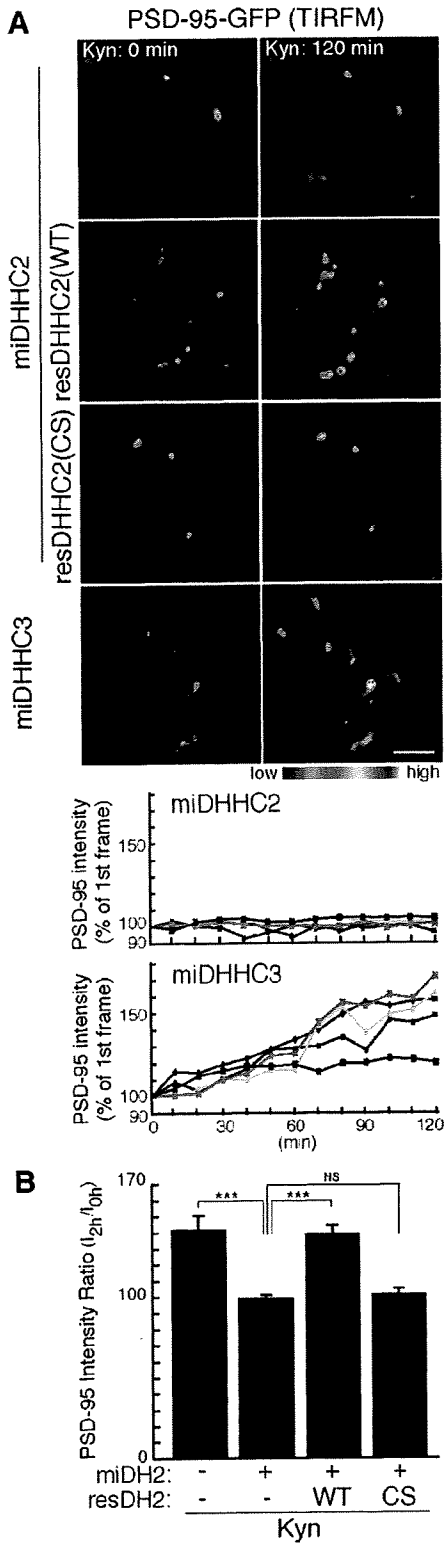

Figure 5. **DHHC2 is essential for activity-sensitive PSD-95 palmitoylation.** (A and B) DHHC2 but not DHHC3 mediates palmitoylation of PSD-95 upon activity blockade. Knockdown of DHHC2 but not DHHC3 inhibited Kyn-induced PSD-95–GFP recruitment at the synaptic membrane. miDHHC2-resistant DHHC2 (WT) but not PAT-inactive DHHC2 (CS) rescued Kyn-induced PSD-95 accumulation. (A) TIRFM intensity of representative five punctae from a neuron was plotted with time. (B) $n = 3$ each; ***, $P < 0.001$. Error bars indicate SD. Bar, 5 μm.

Similar inhibitory effects of DHHC2 or PSD-95 knockdown were observed for endogenous GluR1, GluR2, and TARPs (Fig. S5 G). These results indicate that activity-sensitive PSD-95 palmitoylation by DHHC2 mediates the homeostatic increase of AMPARs.

Discussion

By contrasting two representative PSD-95 palmitoylating enzymes, this study is the first to define differential regulation of DHHC-type palmitoylating enzymes. DHHC3 stably localizes at the Golgi apparatus and constitutively palmitoylates numerous substrates, including Gα, GluR2, and PSD-95. In contrast, dendritically localized DHHC2 senses changes in synaptic activity and rapidly translocates near postsynaptic membranes. Synaptically translocated DHHC2 induces rapid, specific, and stoichiometric palmitoylation and synaptic accumulation of PSD-95 and thereby AMPAR recruitment at postsynaptic sites. Thus, activity-sensitive DHHC2 translocation marks sites for AMPAR accumulation through compartmentalized PSD-95 palmitoylation. Complementing these findings, previous works showed that the *Drosophila melanogaster* DHHC17/HIP14 homologue localizes primarily to presynaptic terminals and acts on presynaptic Cys string protein and SNAP-25 (Ohyama et al., 2007; Stowers and Isacoff, 2007). The DHHC family members show distinctive subcellular distributions and different intracellular dynamics upon physiological stimuli. These distinctive properties provide mechanisms for specific control of protein palmitoylation by the large family of DHHC proteins.

Recent fluorescence recovery after photobleaching and photoconversion analyses revealed that several palmitoylated proteins such as Harvey Ras/neuroblastoma Ras (Rocks et al., 2005), Gαo (Chisari et al., 2007), and Gαq (Tsutsumi et al., 2009) rapidly shuttle between the plasma membrane and the Golgi apparatus. This constitutive shuttling comprises four steps: (1) palmitoylation by the Golgi-resident DHHC proteins, (2) trafficking to the plasma membrane, (3) depalmitoylation by a putative PPT and rapid cytosolic diffusion, and (4) transient trapping at the Golgi for repalmitoylation (Fig. 8 A; Rocks et al., 2006; Tsutsumi et al., 2009). In neurons, where the Golgi apparatus is segregated from the axon and dendrites, we suggest that Golgi-localized DHHC3 mediates the constitutive palmitoylation of PSD-95 at the cell body. In dendrites, PSD-95 depalmitoylated at the postsynaptic membrane diffuses from dendritic spine to shaft, is repalmitoylated on DHHC2-positive vesicles, and is redirected to postsynaptic membranes (Fig. 8 B). When synaptic activity is blocked, DHHC2 vesicles translocate from dendritic shafts to sites near the postsynaptic membrane. This allows DHHC2 to repalmitoylate PSD-95 in the spine (Fig. 8 C). Thus, mobile DHHC2 induces a local increase of PSD-95 palmitoylation, which leads to AMPAR recruitment. We propose that extracellular signals translocate specific DHHC PATs and create a new route for substrate shuttling between loci of palmitoylation and depalmitoylation, leading to efficient and precise substrate targeting. Such a compartmentalized regulatory mechanism of DHHC PATs may contribute to spatiotemporal

Published July 13, 2009

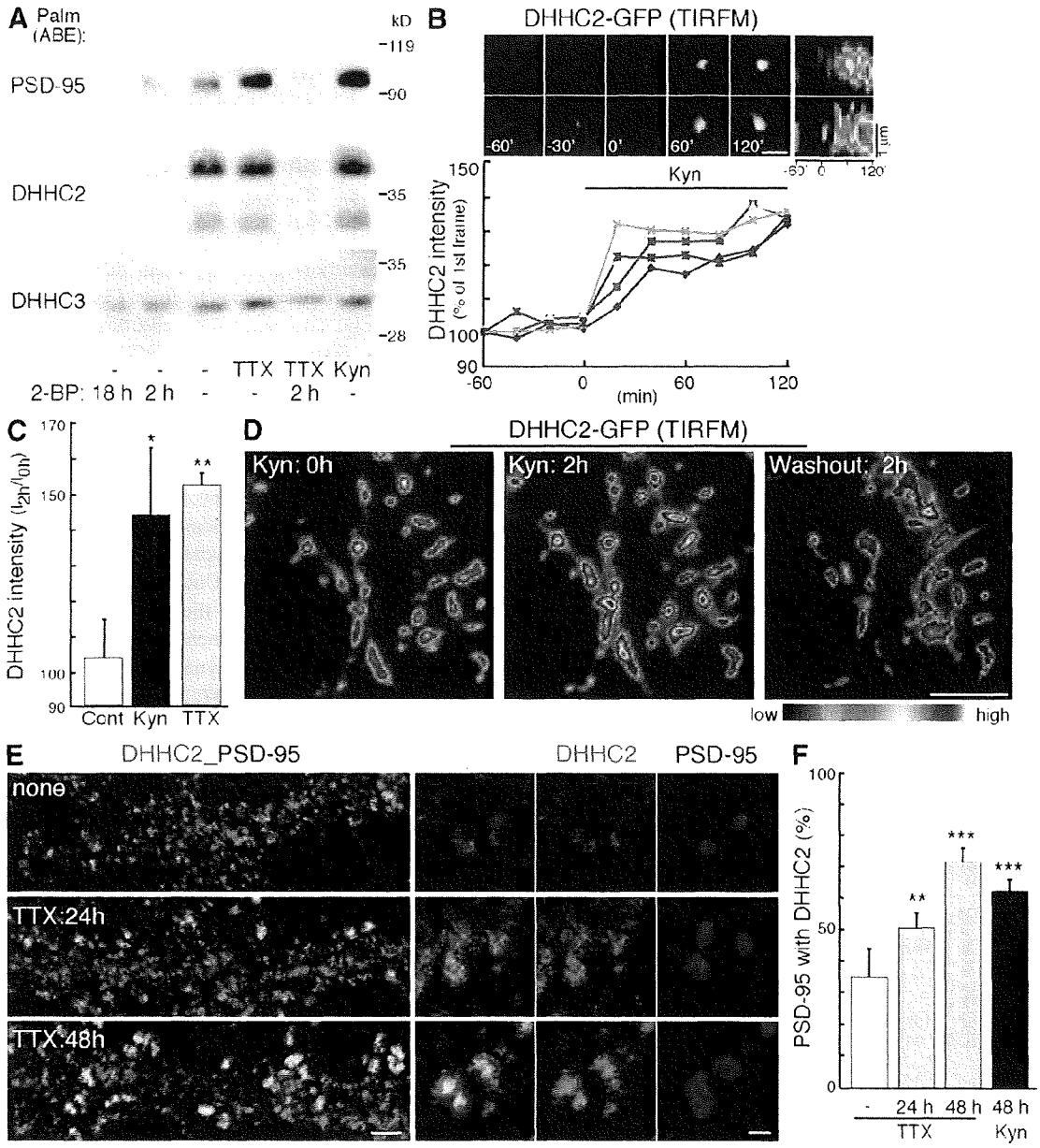

Figure 6. **Activity-sensitive synaptic translocation of DHHC2.** (A) No change in DHHC autopalmitoylation (detected by the ABE method) was seen upon activity blockade (TTX or Kyn) of hippocampal neurons, suggesting that DHHC activity remains constant. (B and C) TIRFM imaging revealed that treatment with Kyn or TTX translocated DHHC2-GFP near the plasma membrane. $n = 3$; *, $P < 0.05$; **, $P < 0.01$ compared with control. Kymographs (pseudocolor) represent the changes in the intensity of DHHC2-GFP over time. (D) The translocation of DHHC2-GFP induced by Kyn treatment was reversible upon washing out Kyn. (E and F) Colocalization of endogenous DHHC2 with PSD-95 steadily increased over prolonged TTX or Kyn treatment. (F) $n = 5$–7 each; **, $P < 0.01$; ***, $P < 0.001$. (C and F) Error bars indicate SD. Bars: (B) 2 μm; (D) 5 μm; (E [left]) 3 μm; (E [right]) 1 μm.

regulation of signaling molecules in polarized neurons, epithelial cells, and migrating cells.

This study monitors intracellular dynamics of palmitoylated proteins by taking advantage of time-lapse TIRFM, which visualizes membrane-associated proteins with exquisite sensitivity. This approach allowed us to follow dynamic changes in membrane-associated PSD-95–GFP over time in individual neurons. However, one may ask whether endogenous PSD-95 shows similar dynamics and whether TIRFM visualizes a limited set of synaptic contacts. The TIRFM limitation was supplemented with epifluorescent and confocal microscopic analyses on endogenous PSD-95. Also, our biochemical approaches, including metabolic labeling and the ABE method, showed that blocking synaptic activity quantitatively increases endogenously palmitoylated PSD-95, supporting the specificity of TIRFM imaging as a method for monitoring palmitoylated proteins in living cells.

A previous study reported that glutamate receptor activation accelerates depalmitoylation of PSD-95, dissociates PSD-95 from postsynaptic sites, and causes AMPAR endocytosis

Published July 13, 2009

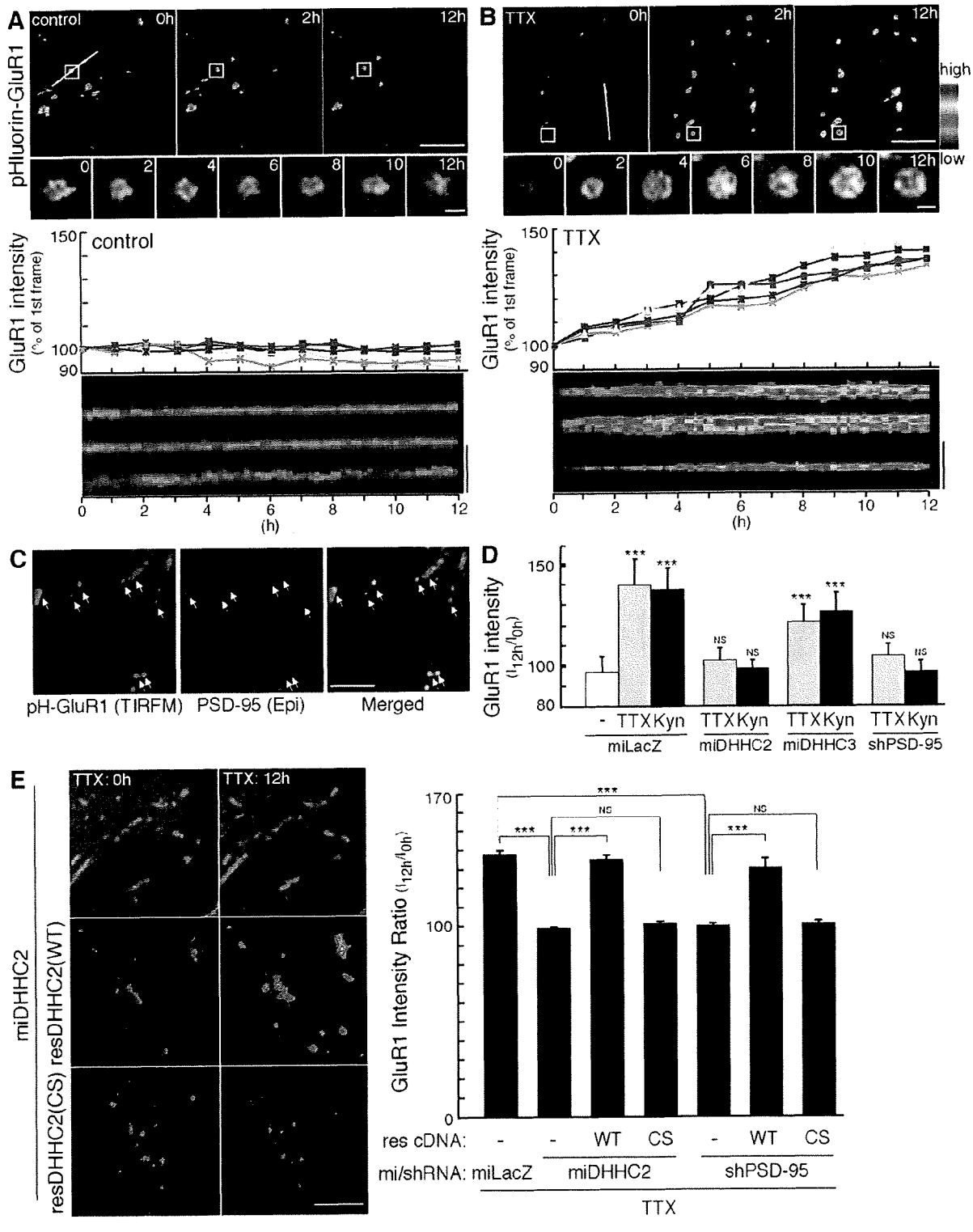

Figure 7. **Essential role of DHHC2-mediated PSD-95 palmitoylation in AMPAR homeostasis.** (A and B) Upon 2 μM TTX treatment, TIRFM intensity of pH-GluR1 punctae gradually and continually increased over a 12-h observation. Fluorescence intensity was displayed in pseudocolor and was plotted with time. Kymographs represent the changes in the intensity of pH-GluR1. White lines indicate the regions used for the kymographs. Insets are magnified in the middle panels. (C) Post hoc immunostaining with PSD-95 showed that all GluR1 punctae by TIRFM overlapped synaptic PSD-95 clusters (arrows). (D) Quantification of fluorescent intensities of pH-GluR1 by TIRFM at 12 h after TTX or Kyn treatment. Knockdown of DHHC2 or PSD-95 completely inhibited the homeostatic increase of surface GluR1. $n = 3$ each; ***, $P < 0.001$ compared with nontreated control. miLacZ is a control miRNA targeting LacZ. (E) The inhibitory effect of DHHC2 knockdown was rescued by miDHHC2-resistant DHHC2 (WT) but not by PAT-inactive DHHC2 (CS). Furthermore, the inhibitory effect of PSD-95 knockdown was rescued by short hairpin RNA–resistant PSD-95 (WT) but not by palmitoylation-deficient PSD-95 (CS). $n = 3$ for each; ***, $P < 0.001$. (D and E) Error bars indicate SD. Bars: (A and B [top] and C) 10 μm; (A and B [insets]) 0.5 μm; (A and B [bottom] and E) 5 μm.

Published July 13, 2009

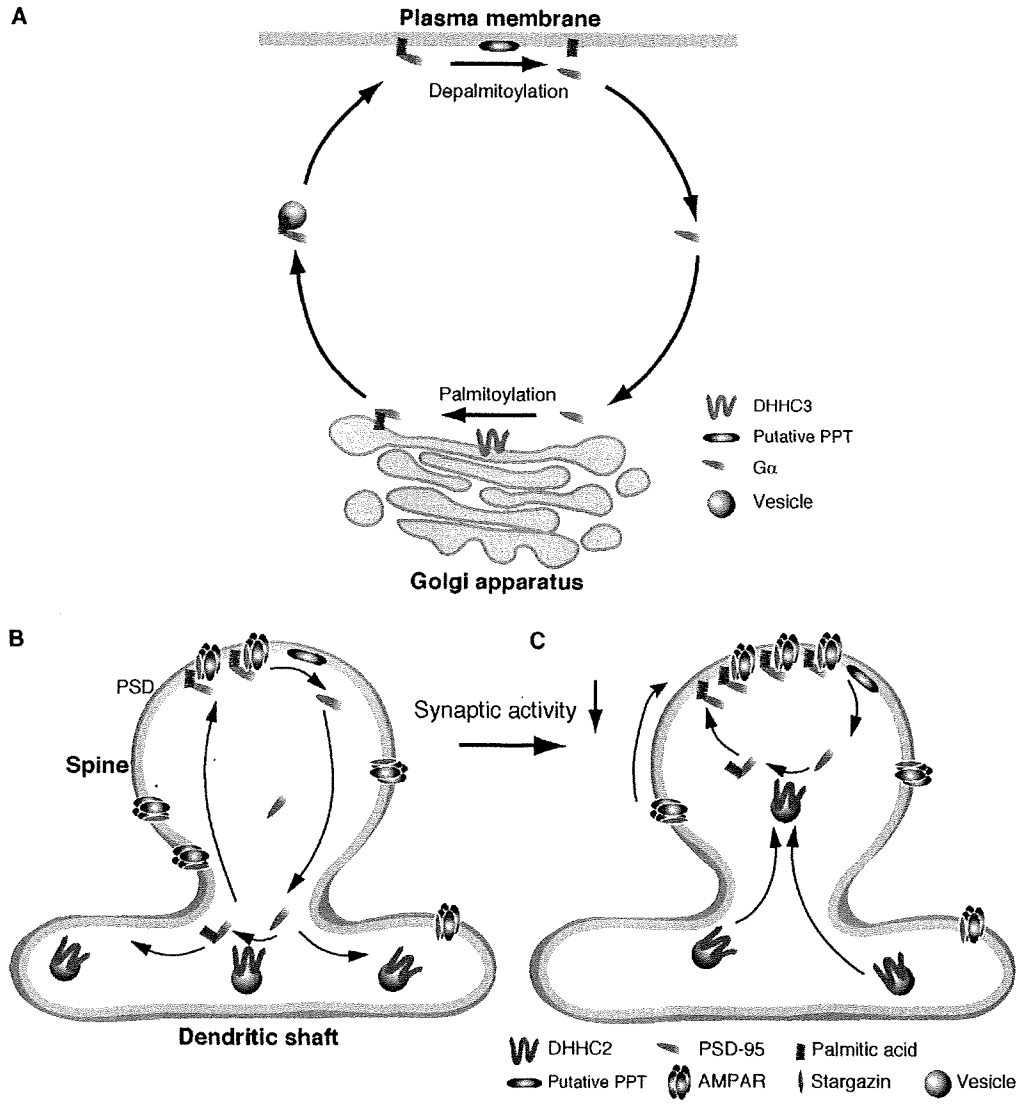

Figure 8. **Model for compartmentalized synaptic palmitoylation of PSD-95 by mobile DHHC2.** (A) Certain palmitoylated proteins such as the Gα subunit shuttle between the plasma membrane and the Golgi in nonpolarized cells. Golgi-resident DHHC3 and a putative PPT at the plasma membrane can mediate this constitutive shuttling. In neurons, DHHC3 localizes at the Golgi apparatus and mediates constitutive palmitoylation of various substrates, including Gα and PSD-95. (B and C) PSD-95 shuttling in dendrites. (B) A dynamic equilibrium exists between palmitoylated postsynaptic PSD-95 and nonpalmitoylated cytosolic PSD-95. Depalmitoylated PSD-95 diffuses into the spine and dendritic shaft. DHHC2 PAT mainly localizes in dendritic shafts on vesicles and mediates dendritic PSD-95 palmitoylation. PSD, postsynaptic density. (C) When synaptic activity is blocked, DHHC2 vesicles move into spines. This translocated DHHC2 palmitoylates spinous PSD-95; the increased postsynaptic PSD-95 thereby contributes to AMPAR homeostasis.

(El-Husseini et al., 2002). This sequence suggested that a PPT serves as the regulatory trigger. In contrast, our work demonstrates that activity blockade–induced PSD-95 palmitoylation up-regulates synaptic AMPARs. Thus, the palmitoylation/depalmitoylation cycle of PSD-95 bidirectionally contributes to AMPAR homeostasis (O'Brien et al., 1998; Turrigiano et al., 1998; Stellwagen and Malenka, 2006). By analogy, β-adrenergic receptor activation markedly accelerates depalmitoylation of Gαs, shifts Gαs to the cytoplasm, and down-regulates β-adrenergic receptor–mediated signaling (Wedegaertner and Bourne, 1994). Collectively, these studies suggest that palmitate cycling may generally mediate homeostasis of receptor-mediated signaling.

Recently, it was shown that both PSD-95 and PSD-93 play important roles in AMPAR trafficking (Elias et al., 2006). In this study, we found that knockdown of PSD-95 alone completely blocks the TTX- or Kyn-induced recruitment of AMPARs to the synapse. One may wonder why knockdown of PSD-95 alone completely blocks the TTX- or Kyn-induced AMPAR recruitment. We quantified expression levels of PSD-95 and PSD-93 in our cultured 18-d in vitro (DIV) hippocampal neurons by quantitative Western blotting. We found that PSD-95 expresses about eight times as much as PSD-93 (Fig. S3 B). Furthermore, we found that PSD-93–β, one of the major PSD-93 isoforms (Firestein et al., 2000; Parker et al., 2004), is specifically palmitoylated by the DHHC3 and -7 subfamily but not

Published July 13, 2009

by the DHHC2 and -15 subfamily (Fig. S3 C), indicating that PSD-93–β palmitoylation is differently regulated from PSD-95 palmitoylation. Furthermore, it was reported that palmitoylation of PSD-93–α and PSD-93–β is not necessary for their postsynaptic targeting (Firestein et al., 2000). Collectively, we conclude that PSD-95 plays a major role in DHHC2-mediated AMPAR recruitment upon activity blockade.

Global proteomic studies indicate that palmitoylation represents a common posttranslational modification (Roth et al., 2006; Kang et al., 2008). Importantly, many palmitoylated proteins are key signaling molecules that subserve physiological processes. Furthermore, mutations of DHHC family members have been detected in cancers (Oyama et al., 2000; Mansilla et al., 2007; Yamamoto et al., 2007) and neurological disorders (Mukai et al., 2004, 2008; Mansouri et al., 2005; Yanai et al., 2006; Raymond et al., 2007). Elucidation of molecular mechanisms for palmitoylation lays a foundation to understand its role in physiological and pathological conditions. Because DHHC enzymes show substrate specificity, DHHC PATs represent exciting therapeutic targets. Our experiments of differential partitioning and regulation on DHHC PATs should serve as a prototype for understanding how dynamic protein palmitoylation is regulated in divergent signaling environments.

Materials and methods

Materials

The following antibodies were used: rabbit polyclonal antibodies to DHHC3/GODZ (Abcam), Gαq (Santa Cruz Biotechnology, Inc.), GluR1 (EMD; Millipore), GRIP1 (Millipore), PSD-93 (Millipore), and stargazin/TARP (Millipore); a guinea pig polyclonal antibody to VGLUT1 (Millipore); and mouse monoclonal antibodies to β-catenin (BD), GluR2 (Millipore), HA (Covance), NMDAR1 (Millipore), PSD-95 (Thermo Fisher Scientific), and synaptophysin (Sigma-Aldrich). Anti–PSD-93 antibody was raised against (aa 336–379) and detected all isoforms of PSD-93. Rabbit polyclonal antibodies to GFP, PSD-95, and moesin were raised against GFP (aa 1–239), GST–PSD-95 (aa 1–434), and GST-moesin (aa 307–577), respectively, and affinity purified. A mouse monoclonal antibody to DHHC2 was raised by a baculovirus display method, which is useful for the production of antibodies against membrane proteins (Masuda et al., 2003; Saitoh et al., 2007). The following reagents were used: Kyn and APV (Tocris); TTX (Nacalai Tesque, Inc.); CNQX and CHX (Sigma-Aldrich); and 2-bromohexadecanoic acid (2-BP; Fluka).

For knockdown experiments in HEK293 cells, siRNAs from QIAGEN were used: scramble (Allstars negative control), siDHHC2, and siDHHC3. siRNA and plasmid-based miRNA for DHHCs were validated by two methods: (1) reduced expression of exogenously expressed DHHC proteins in HEK293 cells (Western blotting) and (2) down-regulation of endogenous mRNAs in HEK293 cells (quantitative real-time PCR).

Cloning and plasmid constructions

The rat cDNAs of synaptophysin (GenBank/EMBL/DDBJ accession no. NM_012664), DHHC2 (GenBank/EMBL/DDBJ accession no. AF228917), DHHC3 (GenBank/EMBL/DDBJ accession no. NM_001039014), DHHC7 (GenBank/EMBL/DDBJ accession no. NM_133394), and DHHC15 (GenBank/EMBL/DDBJ accession no. AY886531) were cloned from rat brain total RNA by RT-PCR. Synaptophysin was subcloned into pCAGGS-GFP, and DHHC2, -3, -7, and -15 were subcloned into pEF-Bos-HA and pcDNA3.1. The mutant rat DHHC2(C156S) was generated by using site-directed mutagenesis. pGW1-rat PSD-95–GFP, pGW1-rat PSD-93–β-GFP and pEF-Bos-HA-mouse DHHC constructs were described previously (El-Husseini et al., 2002; Fukata et al., 2004; Parker et al., 2004). pGW1–PSD-95–HA was constructed by replacing a GFP fragment with a synthetic DNA fragment encoding HA. pEGFP-C1-Rac1-CLLL was described previously (Nakagawa et al., 2001). To obtain the antigen for antibody production, DHHC2 was subcloned into the pcDNA-His-Flag vector. His-Flag–tagged DHHC2 was then subcloned into pAcYM1 for baculovirus production. DHHC2 was also subcloned into pGW1-GFP. To obtain Thy1/pH-GluR1, we first inserted pHluorin between residues 21 and 22 of rat GluR1 (Tomita et al., 2004) and subcloned pH-GluR1 into a Thy1 expression cassette. pCAGGS–pH-GluR2 was made by inserting pHluorin between residues 23 and 24 of mouse GluR2 (Fukata et al., 2005). cDNA of NR2A-GFP (Luo et al., 2002) was subcloned into the pCAGGS vector.

In cultured hippocampal neurons, DHHC2 and -3 were knocked down by the miR-RNAi system (Invitrogen). We used BLOCK-iT RNAi Designer (Invitrogen) to select the targeting sequences, and the following targeting sequences were used (targeting both rat and human sequences): miDHHC2, 5′-GGTGAACAATTGTGTTGGATT-3′ (alternative sequence, 5′-TGTGCATAGTGTCCATGGAAA-3′; both sequences yielded similar results); miDHHC3, 5′-TGAGACGGGAATAGAACAATT-3′; and miLacZ, 5′-GACTACACAAATCAGCGATTT-3′ (as a negative control). After subcloning these oligonucleotides into pcDNA6.2-EmGFP-miR (Invitrogen), EmGFP was replaced with mCherry, and the pre-miRNA expression cassette of pcDNA6.2-mCherry-miR (or pcDNA6.2-EmGFP-miR) was transferred to the pCAGGS vector with a β-actin promoter. PSD-95 was knocked down as described previously (Elias et al., 2006), replacing GFP of pLLox3.7 (American Type Culture Collection) with mCherry. DHHC2 (on pEF-Bos-HA-rat DHHC2) and PSD-95 (on pGW1-rat PSD-95–HA) rescue constructs that have two and four different nucleotides in the target sequences were generated by using site-directed mutagenesis (DHHC2, 5′-GGTGAACAACTGCGTTGGATT-3′; PSD-95, 5′-TCACAATAATAGCCCAGTATA-3′; changed nucleotides are underlined). All PCR products were analyzed by DNA sequencing.

pcDNAI-Gαq-GFP was provided by C.A. Berlot (Weis Center for Research, Danville, PA; Hughes et al., 2001). The cDNAs of pHluorin and mCherry were provided by J.E. Rothman (Columbia University, New York, NY; Miesenbock et al., 1998) and R.Y. Tsien (University of California, San Diego, La Jolla, CA; Shaner et al., 2005), respectively. cDNAs of rat GluR1, NR2A-GFP, and pEGFP-C1-Rac1-CLLL were gifts from R. Huganir (Johns Hopkins University, Baltimore, MD), S. Vicini (Georgetown University School of Medicine, Washington, DC), and K. Kaibuchi (Nagoya University, Showa-Ku, Nagoya, Japan), respectively. Thy1 expression cassette was provided by D. Monard (Friedrich Miescher Institute, Basel, Switzerland; Luthi et al., 1997).

Time-lapse imaging with TIRFM

Hippocampal neuron cultures were prepared from rat embryonic day 18–19 embryos. All animal experiments described herein were reviewed and approved by the ethical committee in our institutes and were performed according to the institutional guidelines concerning the care and handling of experimental animals. Neurons were seeded at a density of 2.5×10^5 cells per 3.5-cm glass-based dish (Iwaki) in neurobasal medium (Invitrogen) supplemented with B-27 supplement (Invitrogen) and 2 mM Glutamax (Invitrogen). 8–10-DIV neurons were transfected by Lipofectamine 2000 (Invitrogen) and observed (18–21 DIV) at 37°C in a microincubator (MI-IBC-IF; Olympus) with an inverted microscope (IX81; Olympus) equipped with a Plan-Apochromat 100× NA 1.45 oil TIRFM objective lens, an ImageEM charge-coupled device (CCD) camera (C9100-13; Hamamatsu Photonics) and Meta Imaging software version 7.1 (MDS Analytical Technologies). A 488-nm laser was used as a light source. Time-lapse images were taken every 10 min with a laser-based zero drift autofocusing system (IX81-ZDC; Olympus), which adjusts the focal plane to the initial focal plane just before each imaging frame. The video files (QuickTime Movie) were produced with ImageReady 2.0 (Adobe Systems, Inc.). To quantitate changes in PSD-95–GFP, DHHC2-GFP, or pH-GluR1 intensity by TIRFM, we randomly chose fields, and the punctae (>1.25 µm in diameter) were quantitated in every frame. Fluorescent intensities from TIRF images were analyzed using MetaMorph software version 7.1 (MDS Analytical Technologies). The ratios of intensities at 0–120 min (for PSD-95 and DHHC2) or 0–12 h (for GluR1) in 50–100 randomly selected punctae (three to eight independent experiments) are shown. Kymographs were produced using Meta Imaging software version 7.1.

Immunofluorescence analysis of hippocampal neuron culture

Cultured hippocampal neurons (5×10^4 cells) were seeded onto 12-mm coverslips in 24-well dishes. 18–28-DIV neurons were fixed with 4% paraformaldehyde/120 mM sucrose/100 mM Hepes, pH 7.4, at room temperature for 10 min, permeabilized with 0.1% Triton X-100 for 10 min, and blocked with PBS containing 10 mg/ml BSA for 10 min on ice. For staining of DHHC2 and VGLUT1, neurons were fixed with methanol for 10 min at −30°C. For mouse anti-DHHC2 antibody, Alexa Fluor 488–conjugated anti–mouse IgG_1 subtype specific (Invitrogen) was used as a secondary antibody. For surface GluR1 and GluR2 staining, GluR1 and GluR2 receptors were "live" labeled with an antibody to an extracellular

Published July 13, 2009

epitope of GluR1 (EMD) or GluR2 (Millipore) by incubating neurons in conditioned medium for 15 min at 37°C. Neurons were then fixed with 2% paraformaldehyde for 20 min and blocked as described above. Surface GluR1 and GluR2 were visualized with Alexa Fluor 488–conjugated secondary antibody. Fluorescent images were taken with a confocal laser-scanning microscopy system (LSM5 Exciter; Carl Zeiss, Inc.) equipped with a Plan-Apochromat 63x NA 1.40 oil immersion objective lens. For knockdown experiments, 8–12-DIV neurons were transfected with pCAGGS-mCherry-miR vectors by Lipofectamine 2000. At 8–10 d after transfection, neurons were stained with anti-DHHC2, DHHC3, PSD-95, GluR1, GluR2, and stargazin/TARP antibodies. To quantitate the intensity of PSD-95 clusters and surface GluR1, surface GluR2, or TARP clusters (costained with PSD-95), we randomly chose 10–15 fields from two independent neuronal cultures (on treated and age-matched sister control cultures) and analyzed the three largest caliber proximal dendrites (20 µm long; at least 400 clusters). We measured the mean intensities of individual clusters (>1 µm diameter) along these dendritic segments. Microscope control and all image analyses were performed with ZEN software (Carl Zeiss, Inc.). Brightness and contrast adjustments were applied to the whole image using Photoshop CS3 (Adobe Systems, Inc.). For some experiments, immunolabeled samples were observed by TIRFM and epifluorescent microscopy.

ABE method

The ABE method was performed as previously described (Roth et al., 2006; Kang et al., 2008) and modified for cultured neurons. After treating 18–28-DIV hippocampal neurons (5×10^5 cells/6-well dish) with the indicated antagonists or inhibitors, neurons were washed with PBS containing 10 mM *N*-ethyl-maleimide (NEM) twice and solubilized with 0.1 ml of lysis buffer (LB; 50 mM Tris-HCl, pH 7.5, 5 mM EDTA, and 50 mM NaCl) containing 2% SDS and 10 mM NEM. After 15 min of extraction, LB with 2% Triton X-100 and 10 mM NEM was added to a final volume of 1 ml and incubated for 1 h at 4°C. After centrifugation at 20,000 *g* for 10 min, the supernatants were precipitated by the chloroform-methanol (CM) method (Wessel and Flugge, 1984). Precipitated protein was solubilized in 0.2 ml SB (50 mM Tris-HCl, pH 7.5, 5 mM EDTA, and 4% SDS) containing 10 mM NEM at 37°C for 10 min. The protein was diluted into 0.8 ml LB with 0.2% Triton X-100 and 1 mM NEM and incubated overnight at 4°C. NEM was removed by three sequential CM precipitations. Precipitated protein was solubilized in 0.2 ml of buffer SB, and then 0.8 ml HB (1 M hydroxylamine, pH 7.5, 150 mM NaCl, 0.2% Triton X-100, and 1 mM biotin-HPDP) or buffer TB (1 M Tris-HCl, pH 7.5, 150 mM NaCl, 0.2% Triton X-100, and 1 mM biotin-HPDP) was added. The mixture was incubated for 1 h at room temperature and subjected to CM precipitation. The precipitated protein was dissolved in 0.2 ml SB, diluted into 0.8 ml LB containing 150 mM NaCl, 0.2% Triton X-100, and 200 µM biotin-HPDP, and incubated for 1 h at room temperature. Free biotin-HPDP was removed by CM precipitation. The precipitated protein was solubilized in 100 µl of buffer UB (50 mM Tris-HCl, pH 7.5, 5 mM EDTA, and 2% SDS) and diluted in 900 µl LB with 0.2% Triton X-100. After brief centrifugation, the supernatant was incubated with 30 µl neutravidin-agarose (Thermo Fisher Scientific) for 1 h at 4°C. After washing the beads with LB containing 0.1% SDS and 0.2% Triton X-100, bound proteins were suspended in SDS-PAGE sample buffer (62.5 mM Tris-HCl, pH 6.8, 10% glycerol, 2% SDS, and 0.001% bromophenol blue) with 10 mM DTT (without βME; −βME) and boiled at 90°C for 2 min. To see the palmitoylation-dependent mobility shift of PSD-95, the cell lysate was treated similarly (−βME). To reduce the sample completely, the lysate was separately treated with SDS-PAGE sample buffer with 2% βME at 100°C for 5 min (+βME). Samples were subjected to SDS-PAGE and Western blotting with the indicated antibodies.

In vivo palmitate labeling

Hippocampal neurons were infected with Semliki forest virus to express GFP or GFP-tagged DN DHHC2/15 (Fukata et al., 2004). At 24 h after infection, cells were labeled for 2 h in neurobasal media containing 3 mCi/ml [^{3}H]palmitic acid (PerkinElmer) either in the presence or absence of 10 mM Kyn. Labeled cells were washed with PBS and resuspended in 0.15 ml LB A (20 mM Tris-HCl, pH 7.5, 1 mM EDTA, 100 mM NaCl, and 1% SDS). After 5 min of extraction, 1% Triton X-100 was added to a final volume of 1.5 ml. After centrifugation at 20,000 *g* for 10 min, the supernatants were incubated with rabbit anti–PSD-95 antibody for 1 h and then incubated for 1 h with 30 µl protein A–Sepharose (GE Healthcare) at 4°C. Immunoprecipitates were washed three times with buffer containing 20 mM Tris-HCl, pH 7.4, 1 mM EDTA, 100 mM NaCl, and 1% Triton X-100. Immunoprecipitated PSD-95 was suspended in SDS sample buffer. For fluorography, protein samples were separated by SDS-PAGE. Gels were treated with Amplify (GE Healthcare) for 30 min, dried under vacuum, and exposed to Biomax MS (Kodak) at −80°C for 2 wk. After autoradiography, the bands were scanned and analyzed with National Institutes of Health software.

Transfected HEK293 cells were preincubated for 30 min in serum-free DME with 5 mg/ml fatty acid–free BSA (Sigma-Aldrich). Cells were then labeled with 0.25 mCi/ml [^{3}H]palmitic acid for 4 h in the preincubation medium. Cells were washed with PBS and scraped with SDS-PAGE sample buffer with 10 mM DTT. The cell lysate was resolved by SDS-PAGE, followed by fluorography (36-h exposure) and Western blotting.

In situ hybridization

In situ hybridization on 7-µm paraffin-embedded 3-wk-old rat brain sections (Genostaff) was performed by using digoxigenin-labeled RNA probes. cDNAs of mouse DHHC2 (nt 1–1,098 from initiating ATG), rat DHHC3 (nt 1–900), rat DHHC7 (nt 1–927), rat DHHC15 (nt 1–1,014), and rat PSD-95 (nt 1,212–1,444) were used for probe templates. An antidigoxigenin antibody linked to alkaline phosphatase (Dako) and NBT/BCIP (nitro blue tetrazolium chloride/5-bromo-4-chloro-3-indolyl phosphate; Dako) substrate was used to detect hybridization signals. All sections were developed for 1 h. Images were taken with a dissection microscope (SZ61; Olympus) equipped with a digital camera (DP20; Olympus) and with an upright microscope (BX51; Olympus) equipped with a UPlan SApo 20x NA 0.75 objective lens and a CCD camera (DP72; Olympus).

Quantitative Western blotting

Bands on blotted membranes were visualized with a cooled CCD camera (Light-Capture II; ATTO), and the optimal specific bands were analyzed with the CS Analyzer 3.0 software (ATTO). For calibration, immunopurified PSD-95–GFP and PSD-93–β-GFP from transfected HEK293 cells were quantitated by Coomassie brilliant staining using BSA.

Subcellular fractionation

The method was basically followed as described previously (Carlin et al., 1980). In brief, five rat adult brains were homogenized in buffer containing 320 mM sucrose and 10 mM Hepes-NaOH, pH 7.4 (containing 0.2 mM PMSF). Homogenate was centrifuged for 10 min at 1,000 *g* to remove crude nuclear fraction (P1). The supernatant (S1) was centrifuged at 9,000 *g* for 15 min to produce a pellet (P2) and supernatant (S2). The S2 was centrifuged at 100,000 *g* for 1 h to produce a pellet (P3; microsomal fraction) and supernatant (S3). The P2 fraction was resuspended in the homogenization buffer. Discontinuous sucrose gradients containing 3 ml of the resuspended P2 material and 3 ml each of 0.8, 1.0, and 1.2 M sucrose solutions in 10 mM Hepes-NaOH, pH 7.4, were run for 2 h at 58,000 *g* (SW41 rotor; Beckman Coulter). The band between 1.0 and 1.2 M sucrose was obtained as a synaptosome fraction. This synaptosome fraction was extracted with ice-cold 0.5% Triton X-100 in 0.16 M sucrose and 6 mM Tris-HCl, pH 8.1, and then centrifuged at 32,800 *g* for 20 min to divide into soluble and insoluble fractions (Ins1; PSD-1). The pellet was resuspended in 0.5% Triton X-100, 0.16 M sucrose, and 6 mM Tris-HCl, pH 8.1, and centrifuged at 200,000 *g* for 1 h to produce a pellet (Ins2; PSD-2). 50 µg of proteins of each fraction was analyzed by Western blotting.

Statistical analysis

The results are expressed as mean ± SD. Statistical comparisons between groups were performed by the Student's *t* test.

Online supplemental material

Fig. S1 shows that synaptic PSD-95 accumulation upon activity blockade does not require protein synthesis. Fig. S2 shows the specific detection of PSD-95 palmitoylation by biochemical approaches. Fig. S3 shows that DHHC2 and -3 and PSD-95 dominantly express as compared with other family proteins in the hippocampus. Fig. S4 shows that DHHC2 translocates near the postsynaptic sites upon activity blockade. Fig. S5 shows that DHHC2 and PSD-95 are necessary for homeostatic increase of GluR2 as well as GluR1. Video 1 shows PSD-95–GFP dynamics in neurons by time-lapse TIRFM imaging and shows the increased accumulation of PSD-95–GFP upon Kyn treatment. Video 2 shows that CHX treatment does not inhibit Kyn-induced PSD-95–GFP increase at the synapse. Video 3 shows that activity-sensitive trafficking of PSD-95 is regulated by DHHC2. Video 4 shows activity-sensitive trafficking of DHHC2. Video 5 shows the specificity of pH-GluR1 imaging. Video 6 shows AMPAR (pH-GluR1) dynamics by time-lapse TIRFM imaging. Video 7 shows that pH-GluR1 intensity gradually and continually increases over 12 h upon TTX treatment. Video 8 shows the

Published July 13, 2009

requirement of palmitoylating activity of DHHC2 for homeostatic increase of GluR1. Video 9 shows the requirement of PSD-95 palmitoylation for the homeostatic increase of GluR1. Online supplemental material is available at http://www.jcb.org/cgi/content/full/jcb.200903101/DC1.

We thank K. Imoto (National Institute for Physiological Sciences, Okazaki, Aichi, Japan) and M. Nishijima (National Institute of Health Sciences, Setagaya-ku,Tokyo, Japan and Japan Science and Technology Agency, Chiyoda-ku, Tokyo, Japan) for suggestions and encouragement, K. Kaibuchi for sharing reagents, F. Perez (Institut Curie, Paris, France), A.S. Kato (Eli Lilly and Company, Indianapolis, IN), and T. Watanabe (Nagoya University, Chikusa-ku, Nagoya, Japan) for valuable suggestions, and N. Takahashi for technical support.

J. Noritake and R. Tsutsumi are supported by the Japan Society for the Promotion of Science. Y. Fukata is supported by grants from the Human Frontier Science Program (HFSP; CDA0015-07) and Ministry of Education, Culture, Sports, Science and Technology (MEXT; 21680029). M. Fukata is also supported by grants from the HFSP (RGY0059-06) and MEXT (20670005, 20022043, and 20054022).

Submitted: 18 March 2009
Accepted: 11 June 2009

References

Ashby, M.C., S.A. De La Rue, G.S. Ralph, J. Uney, G.L. Collingridge, and J.M. Henley. 2004. Removal of AMPA receptors (AMPARs) from synapses is preceded by transient endocytosis of extrasynaptic AMPARs. *J. Neurosci.* 24:5172–5176.

Bartels, D.J., D.A. Mitchell, X. Dong, and R.J. Deschenes. 1999. Erf2, a novel gene product that affects the localization and palmitoylation of Ras2 in *Saccharomyces cerevisiae*. *Mol. Cell. Biol.* 19:6775–6787.

Carlin, R.K., D.J. Grab, R.S. Cohen, and P. Siekevitz. 1980. Isolation and characterization of postsynaptic densities from various brain regions: enrichment of different types of postsynaptic densities. *J. Cell Biol.* 86:831–845.

Chen, L., D.M. Chetkovich, R.S. Petralia, N.T. Sweeney, Y. Kawasaki, R.J. Wenthold, D.S. Bredt, and R.A. Nicoll. 2000. Stargazin regulates synaptic targeting of AMPA receptors by two distinct mechanisms. *Nature.* 408:936–943.

Chisari, M., D.K. Saini, V. Kalyanaraman, and N. Gautam. 2007. Shuttling of G protein subunits between the plasma membrane and intracellular membranes. *J. Biol. Chem.* 282:24092–24098.

El-Husseini, Ael-D., and D.S. Bredt. 2002. Protein palmitoylation: a regulator of neuronal development and function. *Nat. Rev. Neurosci.* 3:791–802.

El-Husseini, A.E., E. Schnell, D.M. Chetkovich, R.A. Nicoll, and D.S. Bredt. 2000. PSD-95 involvement in maturation of excitatory synapses. *Science.* 290:1364–1368.

El-Husseini, Ael-D., E. Schnell, S. Dakoji, N. Sweeney, Q. Zhou, O. Prange, C. Gauthier-Campbell, A. Aguilera-Moreno, R.A. Nicoll, and D.S. Bredt. 2002. Synaptic strength regulated by palmitate cycling on PSD-95. *Cell.* 108:849–863.

Elias, G.M., L. Funke, V. Stein, S.G. Grant, D.S. Bredt, and R.A. Nicoll. 2006. Synapse-specific and developmentally regulated targeting of AMPA receptors by a family of MAGUK scaffolding proteins. *Neuron.* 52:307–320.

Fang, C., L. Deng, C.A. Keller, M. Fukata, Y. Fukata, G. Chen, and B. Luscher. 2006. GODZ-mediated palmitoylation of GABA(A) receptors is required for normal assembly and function of GABAergic inhibitory synapses. *J. Neurosci.* 26:12758–12768.

Fernandez-Hernando, C., M. Fukata, P.N. Bernatchez, Y. Fukata, M.I. Lin, D.S. Bredt, and W.C. Sessa. 2006. Identification of Golgi-localized acyl transferases that palmitoylate and regulate endothelial nitric oxide synthase. *J. Cell Biol.* 174:369–377.

Firestein, B.L., S.E. Craven, and D.S. Bredt. 2000. Postsynaptic targeting of MAGUKs mediated by distinct N-terminal domains. *Neuroreport.* 11:3479–3484.

Fukata, M., Y. Fukata, H. Adesnik, R.A. Nicoll, and D.S. Bredt. 2004. Identification of PSD-95 palmitoylating enzymes. *Neuron.* 44:987–996.

Fukata, Y., A.V. Tzingounis, J.C. Trinidad, M. Fukata, A.L. Burlingame, R.A. Nicoll, and D.S. Bredt. 2005. Molecular constituents of neuronal AMPA receptors. *J. Cell Biol.* 169:399–404.

Fukata, Y., T. Iwanaga, and M. Fukata. 2006. Systematic screening for palmitoyl transferase activity of the DHHC protein family in mammalian cells. *Methods.* 40:177–182.

Funke, L., S. Dakoji, and D.S. Bredt. 2005. Membrane-associated guanylate kinases regulate adhesion and plasticity at cell junctions. *Annu. Rev. Biochem.* 74:219–245.

Hayashi, T., G. Rumbaugh, and R.L. Huganir. 2005. Differential regulation of AMPA receptor subunit trafficking by palmitoylation of two distinct sites. *Neuron.* 47:709–723.

Hemsley, P.A., and C.S. Grierson. 2008. Multiple roles for protein palmitoylation in plants. *Trends Plant Sci.* 13:295–302.

Hemsley, P.A., A.C. Kemp, and C.S. Grierson. 2005. The TIP GROWTH DEFECTIVE1 S-acyl transferase regulates plant cell growth in *Arabidopsis*. *Plant Cell.* 17:2554–2563.

Hughes, T.E., H. Zhang, D.E. Logothetis, and C.H. Berlot. 2001. Visualization of a functional Galpha q-green fluorescent protein fusion in living cells. Association with the plasma membrane is disrupted by mutational activation and by elimination of palmitoylation sites, but not be activation mediated by receptors or AlF4. *J. Biol. Chem.* 276:4227–4235.

Kang, R., J. Wan, P. Arstikaitis, H. Takahashi, K. Huang, A.O. Bailey, J.X. Thompson, A.F. Roth, R.C. Drisdel, R. Mastro, et al. 2008. Neural palmitoyl-proteomics reveals dynamic synaptic palmitoylation. *Nature.* 456:904–909.

Keller, C.A., X. Yuan, P. Panzanelli, M.L. Martin, M. Alldred, M. Sassoe-Pognetto, and B. Luscher. 2004. The gamma2 subunit of GABA(A) receptors is a substrate for palmitoylation by GODZ. *J. Neurosci.* 24:5881–5891.

Kennedy, M.B. 2000. Signal-processing machines at the postsynaptic density. *Science.* 290:750–754.

Kim, E., and M. Sheng. 2004. PDZ domain proteins of synapses. *Nat. Rev. Neurosci.* 5:771–781.

Linder, M.E., and R.J. Deschenes. 2004. Model organisms lead the way to protein palmitoyltransferases. *J. Cell Sci.* 117:521–526.

Linder, M.E., and R.J. Deschenes. 2007. Palmitoylation: policing protein stability and traffic. *Nat. Rev. Mol. Cell Biol.* 8:74–84.

Lobo, S., W.K. Greentree, M.E. Linder, and R.J. Deschenes. 2002. Identification of a Ras palmitoyltransferase in *Saccharomyces cerevisiae*. *J. Biol. Chem.* 277:41268–41273.

Luo, J.H., Z.Y. Fu, G. Losi, B.G. Kim, K. Prybylowski, B. Vissel, and S. Vicini. 2002. Functional expression of distinct NMDA channel subunits tagged with green fluorescent protein in hippocampal neurons in culture. *Neuropharmacology.* 42:306–318.

Luthi, A., H. Van der Putten, F.M. Botteri, I.M. Mansuy, M. Meins, U. Frey, G. Sansig, C. Portet, M. Schmutz, M. Schroder, et al. 1997. Endogenous serine protease inhibitor modulates epileptic activity and hippocampal long-term potentiation. *J. Neurosci.* 17:4688–4699.

Mansilla, F., K. Birkenkamp-Demtroder, M. Kruhoffer, F.B. Sorensen, C.L. Andersen, P. Laiho, L.A. Aaltonen, H.W. Verspaget, and T.F. Orntoft. 2007. Differential expression of DHHC9 in microsatellite stable and instable human colorectal cancer subgroups. *Br. J. Cancer.* 96:1896–1903.

Mansouri, M.R., L. Marklund, P. Gustavsson, E. Davey, B. Carlsson, C. Larsson, I. White, K.H. Gustavson, and N. Dahl. 2005. Loss of ZDHHC15 expression in a woman with a balanced translocation t(X;15)(q13.3;cen) and severe mental retardation. *Eur. J. Hum. Genet.* 13:970–977.

Masuda, K., H. Itoh, T. Sakihama, C. Akiyama, K. Takahashi, R. Fukuda, T. Yokomizo, T. Shimizu, T. Kodama, and T. Hamakubo. 2003. A combinatorial G protein-coupled receptor reconstitution system on budded baculovirus. Evidence for Galpha and Galphao coupling to a human leukotriene B4 receptor. *J. Biol. Chem.* 278:24552–24562.

Miesenbock, G., D.A. De Angelis, and J.E. Rothman. 1998. Visualizing secretion and synaptic transmission with pH-sensitive green fluorescent proteins. *Nature.* 394:192–195.

Migaud, M., P. Charlesworth, M. Dempster, L.C. Webster, A.M. Watabe, M. Makhinson, Y. He, M.F. Ramsay, R.G. Morris, J.H. Morrison, et al. 1998. Enhanced long-term potentiation and impaired learning in mice with mutant postsynaptic density-95 protein. *Nature.* 396:433–439.

Mukai, J., H. Liu, R.A. Burt, D.E. Swor, W.S. Lai, M. Karayiorgou, and J.A. Gogos. 2004. Evidence that the gene encoding ZDHHC8 contributes to the risk of schizophrenia. *Nat. Genet.* 36:725–731.

Mukai, J., A. Dhilla, L.J. Drew, K.L. Stark, L. Cao, A.B. MacDermott, M. Karayiorgou, and J.A. Gogos. 2008. Palmitoylation-dependent neurodevelopmental deficits in a mouse model of 22q11 microdeletion. *Nat. Neurosci.* 11:1302–1310.

Nakagawa, M., M. Fukata, M. Yamaga, N. Itoh, and K. Kaibuchi. 2001. Recruitment and activation of Rac1 by the formation of E-cadherin-mediated cell-cell adhesion sites. *J. Cell Sci.* 114:1829–1838.

Nicoll, R.A., S. Tomita, and D.S. Bredt. 2006. Auxiliary subunits assist AMPA-type glutamate receptors. *Science.* 311:1253–1256.

O'Brien, R.J., S. Kamboj, M.D. Ehlers, K.R. Rosen, G.D. Fischbach, and R.L. Huganir. 1998. Activity-dependent modulation of synaptic AMPA receptor accumulation. *Neuron.* 21:1067–1078.

Ohyama, T., P. Verstreken, C.V. Ly, T. Rosenmund, A. Rajan, A.C. Tien, C. Haueter, K.L. Schulze, and H.J. Bellen. 2007. Huntingtin-interacting

Published July 13, 2009

protein 14, a palmitoyl transferase required for exocytosis and targeting of CSP to synaptic vesicles. *J. Cell Biol.* 179:1481–1496.

Oyama, T., Y. Miyoshi, K. Koyama, H. Nakagawa, T. Yamori, T. Ito, H. Matsuda, H. Arakawa, and Y. Nakamura. 2000. Isolation of a novel gene on 8p21.3-22 whose expression is reduced significantly in human colorectal cancers with liver metastasis. *Genes Chromosomes Cancer.* 29:9–15.

Parker, M.J., S. Zhao, D.S. Bredt, J.R. Sanes, and G. Feng. 2004. PSD93 regulates synaptic stability at neuronal cholinergic synapses. *J. Neurosci.* 24:378–388.

Ponimaskin, E., G. Dityateva, M.O. Ruonala, M. Fukata, Y. Fukata, F. Kobe, F.S. Wouters, M. Delling, D.S. Bredt, M. Schachner, and A. Dityatev. 2008. Fibroblast growth factor-regulated palmitoylation of the neural cell adhesion molecule determines neuronal morphogenesis. *J. Neurosci.* 28:8897–8907.

Raymond, F.L., P.S. Tarpey, S. Edkins, C. Tofts, S. O'Meara, J. Teague, A. Butler, C. Stevens, S. Barthorpe, G. Buck, et al. 2007. Mutations in ZDHHC9, which encodes a palmitoyltransferase of NRAS and HRAS, cause X-linked mental retardation associated with a Marfanoid habitus. *Am. J. Hum. Genet.* 80:982–987.

Resh, M.D. 2006. Palmitoylation of ligands, receptors, and intracellular signaling molecules. *Sci. STKE.* doi:10.1126/stke.3592006re14.

Rocks, O., A. Peyker, M. Kahms, P.J. Verveer, C. Koerner, M. Lumbierres, J. Kuhlmann, H. Waldmann, A. Wittinghofer, and P.I. Bastiaens. 2005. An acylation cycle regulates localization and activity of palmitoylated Ras isoforms. *Science.* 307:1746–1752.

Rocks, O., A. Peyker, and P.I. Bastiaens. 2006. Spatio-temporal segregation of Ras signals: one ship, three anchors, many harbors. *Curr. Opin. Cell Biol.* 18:351–357.

Roth, A.F., Y. Feng, L. Chen, and N.G. Davis. 2002. The yeast DHHC cysteine-rich domain protein Akr1p is a palmitoyl transferase. *J. Cell Biol.* 159:23–28.

Roth, A.F., J. Wan, A.O. Bailey, B. Sun, J.A. Kuchar, W.N. Green, B.S. Phinney, J.R. Yates III, and N.G. Davis. 2006. Global analysis of protein palmitoylation in yeast. *Cell.* 125:1003–1013.

Saitoh, R., T. Ohtomo, Y. Yamada, N. Kamada, J. Nezu, N. Kimura, S. Funahashi, K. Furugaki, T. Yoshino, Y. Kawase, et al. 2007. Viral envelope protein gp64 transgenic mouse facilitates the generation of monoclonal antibodies against exogenous membrane proteins displayed on baculovirus. *J. Immunol. Methods.* 322:104–117.

Shaner, N.C., P.A. Steinbach, and R.Y. Tsien. 2005. A guide to choosing fluorescent proteins. *Nat. Methods.* 2:905–909.

Stellwagen, D., and R.C. Malenka. 2006. Synaptic scaling mediated by glial TNF-alpha. *Nature.* 440:1054–1059.

Stowers, R.S., and E.Y. Isacoff. 2007. *Drosophila* huntingtin-interacting protein 14 is a presynaptic protein required for photoreceptor synaptic transmission and expression of the palmitoylated proteins synaptosome-associated protein 25 and cysteine string protein. *J. Neurosci.* 27:12874–12883.

Tomita, S., M. Fukata, R.A. Nicoll, and D.S. Bredt. 2004. Dynamic interaction of stargazin-like TARPs with cycling AMPA receptors at synapses. *Science.* 303:1508–1511.

Topinka, J.R., and D.S. Bredt. 1998. N-terminal palmitoylation of PSD-95 regulates association with cell membranes and interaction with K+ channel, Kv1.4. *Neuron.* 20:125–134.

Tsutsumi, R., Y. Fukata, J. Noritake, T. Iwanaga, F. Perez, and M. Fukata. 2009. Identification of G protein alpha subunit-palmitoylating enzyme. *Mol. Cell. Biol.* 29:435–447.

Turrigiano, G.G., K.R. Leslie, N.S. Desai, L.C. Rutherford, and S.B. Nelson. 1998. Activity-dependent scaling of quantal amplitude in neocortical neurons. *Nature.* 391:892–896.

Wedegaertner, P.B., and H.R. Bourne. 1994. Activation and depalmitoylation of Gs alpha. *Cell.* 77:1063–1070.

Wessel, D., and U.I. Flugge. 1984. A method for the quantitative recovery of protein in dilute solution in the presence of detergents and lipids. *Anal. Biochem.* 138:141–143.

Yamamoto, Y., Y. Chochi, H. Matsuyama, S. Eguchi, S. Kawauchi, T. Furuya, A. Oga, J.J. Kang, K. Naito, and K. Sasaki. 2007. Gain of 5p15.33 is associated with progression of bladder cancer. *Oncology.* 72:132–138.

Yanai, A., K. Huang, R. Kang, R.R. Singaraja, P. Arstikaitis, L. Gan, P.C. Orban, A. Mullard, C.M. Cowan, L.A. Raymond, et al. 2006. Palmitoylation of huntingtin by HIP14 is essential for its trafficking and function. *Nat. Neurosci.* 9:824–831.

Yudowski, G.A., M.A. Puthenveedu, D. Leonoudakis, S. Panicker, K.S. Thorn, E.C. Beattie, and M. von Zastrow. 2007. Real-time imaging of discrete exocytic events mediating surface delivery of AMPA receptors. *J. Neurosci.* 27:11112–11121.

JOURNAL OF VIROLOGY, May 2009, p. 5137–5147 Vol. 83, No. 10
0022-538X/09/$08.00+0 doi:10.1128/JVI.02179-08

Involvement of Creatine Kinase B in Hepatitis C Virus Genome Replication through Interaction with the Viral NS4A Protein▽

Hiromichi Hara,[1,2] Hideki Aizaki,[1] Mami Matsuda,[1] Fumiko Shinkai-Ouchi,[3] Yasushi Inoue,[1,4] Kyoko Murakami,[1] Ikuo Shoji,[1,5] Hayato Kawakami,[6] Yoshiharu Matsuura,[7] Michael M. C. Lai,[8] Tatsuo Miyamura,[1] Takaji Wakita,[1] and Tetsuro Suzuki[1]*

Department of Virology II[1] and Department of Biochemistry and Cell Biology,[3] National Institute of Infectious Diseases, Tokyo 162-8640, Japan; Department of Internal medicine, Division of Pulmonary Diseases, The Jikei University School of Medicine, Tokyo 105-8461, Japan[2]; Mita Hospital, International University of Health and Welfare, Tokyo 108-8329, Japan[4]; Division of Microbiology, Kobe University Graduate School of Medicine, Hyogo 650-0017, Japan[5]; Department of Anatomy, Kyorin University School of Medicine, Tokyo 181-8611, Japan[6]; Research Institute for Microbial Diseases, Osaka University, Osaka 565-0871, Japan[7]; and Department of Molecular Microbiology and Immunology, University of Southern California, Keck School of Medicine, Los Angeles, California 90033[8]

Received 15 October 2008/Accepted 20 February 2009

Persistent infection with hepatitis C virus (HCV) is a major cause of chronic liver diseases. The aim of this study was to identify host cell factor(s) participating in the HCV replication complex (RC) and to clarify the regulatory mechanisms of viral genome replication dependent on the host-derived factor(s) identified. By comparative proteome analysis of RC-rich membrane fractions and subsequent gene silencing mediated by RNA interference, we identified several candidates for RC components involved in HCV replication. We found that one of these candidates, creatine kinase B (CKB), a key ATP-generating enzyme that regulates ATP in subcellular compartments of nonmuscle cells, is important for efficient replication of the HCV genome and propagation of infectious virus. CKB interacts with HCV NS4A protein and forms a complex with NS3-4A, which possesses multiple enzyme activities. CKB upregulates both NS3-4A-mediated unwinding of RNA and DNA in vitro and replicase activity in permeabilized HCV replicating cells. Our results support a model in which recruitment of CKB to the HCV RC compartment, which has high and fluctuating energy demands, through its interaction with NS4A is important for efficient replication of the viral genome. The CKB-NS4A association is a potential target for the development of a new type of antiviral therapeutic strategy.

Hepatitis C virus (HCV) infection represents a significant global healthcare burden, and current estimates suggest that a minimum of 3% of the world's population is chronically infected (4, 19). The virus is responsible for many cases of severe chronic liver diseases, including cirrhosis and hepatocellular carcinoma (4, 16, 19). HCV is a positive-stranded RNA virus belonging to the family *Flaviviridae*. Its ~9.6-kb genome is translated into a single polypeptide of about 3,000 amino acids (aa), in which the nonstructural (NS) proteins NS2, NS3, NS4A, NS4B, NS5A, and NS5B reside in the C-terminal half region (6, 34, 44). NS4A, a small 7-kDa protein, functions as a cofactor for NS3 to enhance NS3 enzyme activities such as serine protease and helicase activities. The hydrophobic N-terminal region of NS4A, which is predicted to form a transmembrane α-helix, is responsible for membrane anchorage of the NS3-4A complex (8, 44, 50), and the central region of NS4A is important for the interaction with NS3 (10, 44). A recent study demonstrated the involvement of the C terminus of NS4A in the regulation of NS5A hyperphosphorylation and viral replication (28).

The development of HCV replicon technology several years ago accelerated research on viral RNA replication (7, 44). Furthermore, a robust cell culture system for propagation of infectious HCV particles was developed using a viral genome of HCV genotype 2a, JFH-1 strain, enabling us to study every process in the viral life cycle (27, 47, 54). RNA derived from genotype 1a, HCV H77, containing cell-culture adaptive mutations, also produces infectious viruses (52). Using these systems, it has been reported that the HCV genome replicates in a distinct, subcellular replication complex (RC) compartment, which includes NS3-5B and the viral RNA (2, 14, 33). The RC forms in a distinct compartment with high concentrations of viral and cellular components located on detergent-resistant membrane (DRM) structures, possibly a lipid-raft structure (2, 41), which may protect the RC from external proteases and nucleases. Almost all processes in viral replication are dependent on the host cell's machinery and involve intimate interaction between viral and host proteins. However, the functional roles of host factors interacting with the HCV RC in viral genome replication remain ambiguous.

To gain a better understanding of cellular factors that are components of the HCV RC and that function as regulators of viral replication, a comparative proteomic analysis of DRM fractions from HCV replicon and parental cells and subsequent RNA interference (RNAi) silencing of selected genes were performed. We identified creatine kinase B (CKB) as a key factor for the HCV genome replication. CKB catalyzes the reversible transfer of the phosphate group of phosphocreatine

* Corresponding author. Mailing address: Department of Virology II, National Institute of Infectious Diseases, 1-23-1 Toyama, Shinjuku-ku, Tokyo 162-8640, Japan. Phone: 81-3-5285-1111. Fax: 81-3-5285-1161. E-mail: tesuzuki@nih.go.jp.

▽ Published ahead of print on 4 March 2009.

(pCr) to ADP to yield ATP and creatine and is known to play important roles in local delivery and cellular compartmentalization of ATP (48, 51). The findings obtained here suggest that recruitment of CKB to the HCV RC, through CKB interaction with NS4A, is essential for maintenance or enhancement of viral replicase activity.

MATERIALS AND METHODS

Cell lines, antibodies, and reagents. Human hepatoma cell line Huh-7.5.1 (54) was kindly provided by Francis V. Chisari. Cell lines carrying subgenomic replicon RNAs, namely, SGR-N (41) and SGR-JFH1 (23), were derived from the HCV-N (17) and JFH-1 strains (24), respectively. Mouse monoclonal antibodies (MAbs) against HCV NS3 (Chemicon, Temecula, CA), NS4A (Santa Cruz Biotechnology, Inc., Santa Cruz, CA), NS5A (Biodesign, Saco, ME), NS5B (2), FLAG (M2; Sigma-Aldrich, St. Louis, MO), glyceraldehyde-3-phosphate dehydrogenase (GAPDH; Chemicon), and Flotillin-1 (BD Biosciences, San Jose, CA) and polyclonal antibodies (PAbs) against CKB (mouse [Abnova, Taipei, Taiwan], goat [Santa Cruz]), hemagglutinin (HA; Sigma-Aldrich), and FLAG (Sigma-Aldrich) were used. Cyclocreatine (Ccr; also known as 2-imino-1-imidazolidineacetic acid), pCr, and phosphopyruvic acid (pPy) were purchased from Sigma-Aldrich. Recombinant CKB and pyruvate kinase (PK) were obtained from Acris (Herfold, Germany) and Calbiochem (San Diego, CA), respectively.

Proteome analysis. RC-rich membrane fractions of cells were isolated as described previously (2, 41). Briefly, cells were lysed in hypotonic buffer. After removing the nuclei, supernatants were treated with 1% NP-40 for 60 min, mixed with 70% sucrose, overlaid with 55 and 10% sucrose, and centrifuged at 38,000 rpm for 14 h. Proteins from membrane fractions were purified by using a 2D Clean-Up kit (GE Healthcare, Tokyo, Japan), followed by labeling with fluorescent dyes: Cy5 for replicon cells, Cy3 for parental cells, and Cy2 for the protein standard containing equal amounts of both cell samples. Two-dimensional fluorescence difference gel electrophoresis (2D-DIGE) was performed using Immobiline DryStrip as the first-dimension gel and 12.5% polyacrylamide gel as the second-dimension gel. The 2D-DIGE images were analyzed quantitatively using the DeCyder software (GE Healthcare). Student *t* test was performed on differences between the tested samples using DeCyder biological variation analysis module. Samples were analyzed in triplicate. The protein spots of interest were excised from the gel, subjected to in-gel digestion using trypsin or lysyl endopeptidase and analyzed by liquid chromatography (MAGIC 2002 System; Michrom Bioresources, Auburn, CA) directly connected to electrospray ionization-ion trap mass spectrometry (LCQ-decaXP; Thermo Electron Corp., Iwakura, Japan). The results were subjected to database (NCBInr) search by Mascot server software (Matrix Science, Boston, MA) for peptide assignment.

Plasmids. A human CKB cDNA (43; kindly provided by Oriental Yeast Corp., Tokyo, Japan) was inserted into the EcoRI site of pCAGGS, yielding pCAGCKB. To generate expression plasmids for HA-tagged versions of wild-type and deletion mutated CKB, the corresponding DNA fragments were amplified by PCR, followed by introduction into the BglII site of pCAGGS. A fragment representing the inactive mutant CKB-C283S was synthesized by PCR mutagenesis. To generate FLAG-tagged NS protein expression plasmids, DNA fragments encoding either NS3, NS4A, NS4B, NS5A, or NS5B protein were amplified from HCV strains NIHJ1 (1) and JFH-1 (23) by PCR, followed by cloning into the EcoRI-EcoRV sites of pcDNA3-MEF (20). To generate an HA-tagged NS3 expression plasmid, a fragment encoding NS3 with the HA tag sequence at its N terminus was inserted into pCAGGS.

siRNA transfection. The small interfering RNAs (siRNAs) targeted to CKB (CKB-1 [5′-UAAGACCUUCCUGGUGUGGTT-3′] and CKB-2 [5′-CGUCAC CCUUGGUAGAGUUTT-3′]) and the scramble negative control siRNA to CKB-2 (5′-GGCGUACUAGCUUAUUCGCTT-3′) were purchased from Sigma. Cells in a 24-well plate were transfected with siRNA using HiPerFect transfection reagent (Qiagen, Tokyo, Japan) according to the manufacturer's instructions. The siRNA sequences for the other genes used in the siRNA screening are available upon request.

HCV infection. Culture media from Huh-7 cells transfected with in vitro-transcribed RNA corresponding to the full-length JFH-1 (47) was collected, concentrated, and used for the infection assay (3).

Quantification of HCV core protein and RNA. To estimate the levels of HCV core protein, aliquots of culture supernatants or of cell lysates were assayed by using HCV Core enzyme-linked immunosorbent assay kits (5). Total RNA was isolated from harvested cells using TRIzol (Invitrogen, Carlsbad, CA). Copy numbers of the viral RNA were determined by reverse transcription-PCR (RT-PCR) (2, 36, 46).

Immunoprecipitation, immunoblot analysis, and immunofluorescence microscopy. The analyses, as well as DNA transfection, were performed essentially as previously described (42). Cells were lysed in immunoprecipitation lysis buffer (50 mM Tris-HCl [pH 7.6], 150 mM NaCl, 1% sodium deoxycholate, 1% NP-40, 0.1% sodium dodecyl sulfate, 1 mM dithiothreitol, 1 mM calcium acetate). For immunoprecipitation, supernatants of cell lysates were precipitated with anti-FLAG antibody and protein A-Sepharose Fast Flow beads (GE healthcare). For immunofluorescence microscopy, anti-CKB goat PAb and anti-NS4A MAb as primary antibodies and Alexa Fluor 555-conjugated donkey anti-goat immunoglobulin G (Invitrogen) and Alexa Fluor 488-conjugated rabbit anti-mouse immunoglobulin G (Invitrogen) as secondary antibodies were used and observed under an LSM 510 confocal microscope (Carl Zeiss, Oberkochen, Germany).

Immunoelectron microscopy. Postembedding immunostaining using the colloidal gold-labeling method was performed as described previously (38). Cells were fixed in 4% paraformaldehyde–1% glutaraldehyde at 4°C for 1 h. After dehydration through a graded series of ethanol, cells were embedded in LR White (London Resin Company, London, United Kingdom) and sectioned. After blocking, section grids were incubated with a mixture of anti-NS4A and anti-CKB antibodies at 4°C overnight, followed by treatment with a mixture of 18-nm colloidal gold-conjugated donkey anti-mouse immunoglobulin G and 12-nm colloidal gold-conjugated donkey anti-goat immunoglobulin G antibodies (Jackson Immunoresearch, West Grove, PA) at 4°C overnight. The sections were stained with uranyl acetate and observed under a transmission electron microscope.

Measurement of CK activity and cellular ATP level. Cells were lysed with passive lysis buffer (Promega, Madison, WI), and CK activities were measured based on Oliver methods (40), in which the activity of converting creatine phosphate and ADP to creatine and ATP was measured. ATP levels in cell lysates were measured by using a CellTiter-Glo luminescent cell viability assay (Promega).

RNA replication assays in permeabilized replicon cells and in vitro. The RNA synthesis assay using permeabilized replicon cells was based on a previously described method (33). Briefly, SGR-JFH1 cells were treated with 5 μg of actinomycin D/ml for 2 h, followed by permeabilization with 50 μg of digitonin/ml for 5 min. The resulting mix was incubated with 500 μM concentrations of ATP, GTP, and CTP; 10 μCi of UTP ([α-^{32}P]UTP); 50 μg of actinomycin D/ml; and 5 mM pCr with or without 20 U of CKB/ml for 4 h at 27°C. RNA was extracted by using TRIzol and analyzed by 1% formaldehyde agarose gel electrophoresis. The cell-free RNA replication assay was performed as described previously (2).

In vitro helicase assays. Helicase activity on double-stranded RNA (dsRNA) was investigated as described previously (11) with some modifications. The 5′ end of the release strand was labeled with [γ-^{32}P]ATP using T4 polynucleotide kinase (Ambion). The dsRNA substrate was obtained by annealing the labeled RNA with a template strand RNA at a molar ratio of 1:1. The helicase assay mixture contained 5 nM dsRNA, helicase enzyme (80 nM NS3 or NS3-4A [kindly provided by R. De Francesco]), 6 mM ATP, in the presence or absence of 20 U of CKB/ml in an assay buffer (25 mM MOPS-NaOH [pH 7.0], 2.5 mM dithiothreitol, 100 μg of bovine serum albumin/ml, 3 mM $MgCl_2$, 5 mM pCr, 2.5 U of RNase inhibitor/ml). After the helicase reaction, samples were electrophoresed in a native 8% polyacrylamide gel and autoradiographed.

To determine the effect of PK/pPy system on the helicase activity, PK and pPy were used instead of CKB and pCr. Helicase activity on dsDNA was measured based on homogeneous time-resolved fluorescence quenching using a Trupoint helicase assay kit (Perkin-Elmer, Waltham, MA) according to the manufacturer's instructions.

In vitro protease assay. In vitro HCV protease activity of NS3-4A or NS3 was analyzed by using a SensoLyteHCV protease assay kit (AnaSpec, San Jose, CA) according to the manufacturer's instructions.

RESULTS

Identification of host factors involved in HCV RNA replication by comparative proteomic analysis of DRM fractions and RNAi silencing. To identify host proteins involved in the HCV RC, proteome profiles of the RC-rich membrane fraction in Huh-7 cells harboring subgenomic replicon RNA derived from genotype 1b, N isolate (SGR-N) were compared to those of parental cells by 2D-DIGE. We confirmed that the DRM fraction obtained from SGR-N cells is functionally active in a

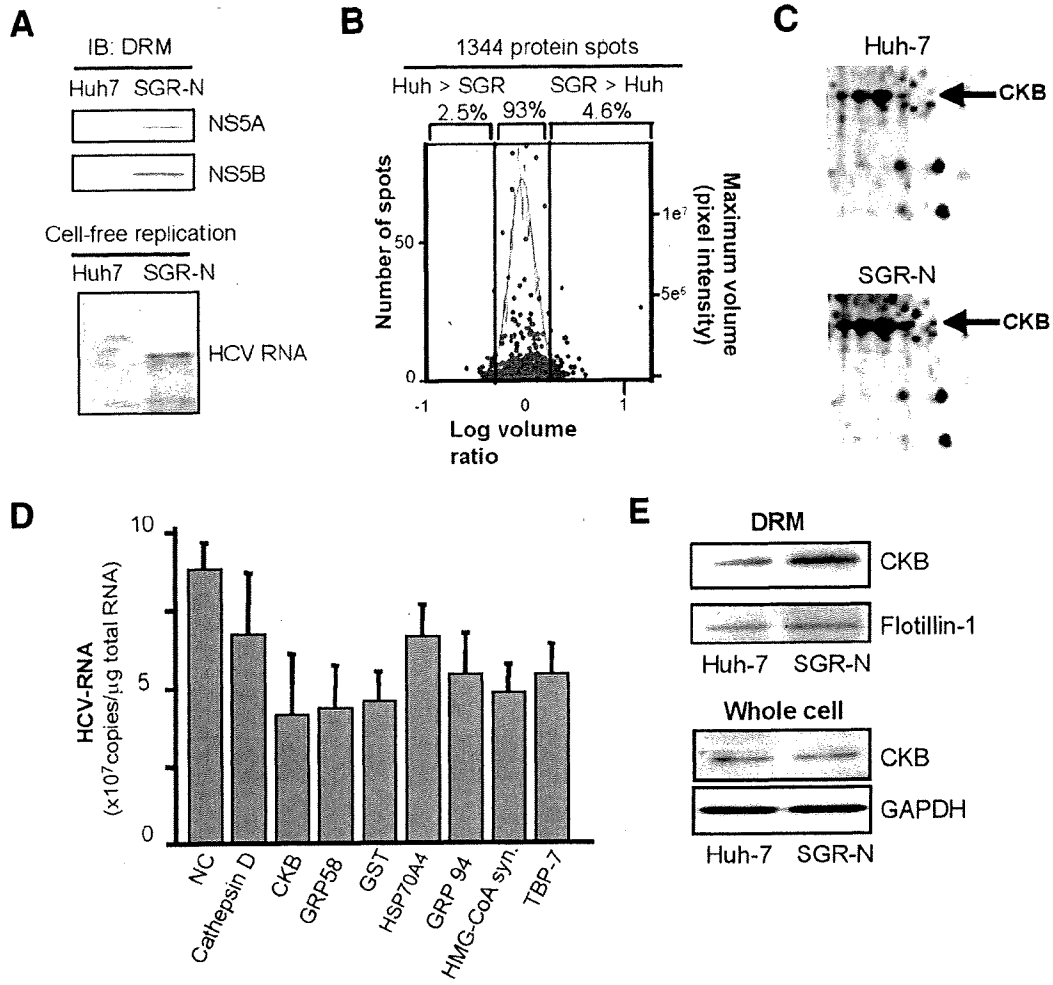

FIG. 1. Comparative proteomic analysis of DRM fractions and RNAi silencing. (A) Preparation of functionally active RC fraction for proteome analysis. DRM fractions obtained from SGR-N cells and parental Huh-7 cells were analyzed by immunoblotting with anti-NS5A and anti-NS5B antibodies (upper panel) and by the cell-free RNA replication assay (lower panel). (B) Histogram representation of proteins detected in 2D-DIGE. Images were analyzed quantitatively by the DeCyder software. The left and right *y* axis, respectively, indicate the spot frequency and the maximum volume of each spot, given against the log volume ratio (*x* axis). (C) Comparison of 2D-DIGE maps of proteins from DRM fractions of SGR-N cells and Huh-7 cells. Enlarged 2D-DIGE gel images of regions containing protein spots of CKB (arrows) are shown. (D) Effects of siRNAs of genes selected from comparative proteome analysis on HCV RNA replication. SGR-N cells were transfected with siRNA specific to cathepsin D, CKB (siCKB-1), GRP58, GST, Hsp70 protein 4, GRP94, HMG-coenzyme A synthase, or Tat binding protein 7 or with nontargeting (NC) siRNA. At 48 h posttransfection, total RNA was isolated and HCV RNA levels were assessed by real-time RT-PCR. (E) Enrichment of CKB in the DRM of HCV replicon cells. Equal amounts of DRM fractions from SGR-N and parental Huh-7 cells, or whole-cell lysates from both cells were analyzed by immunoblotting with antibodies against CKB, flotilin-1 or GAPDH.

cell-free replication assay (Fig. 1A). Three independent proteome experiments were performed for a reliable analysis of protein expression. Approximately 1,300 spots were resolved in each gel, and 4 to 5% of the protein spots represented a >2-fold increase in the membrane fraction of replicon cells in each experiment (Fig. 1B). The protein spots that exhibited high reproducibility (an example shown in Fig. 1C) were excised, digested by trypsin or lysyl endopeptidase, and analyzed by mass spectrometry, which identified the corresponding proteins in 27 cases (Table 1). Among the proteins implicated in a variety of functional categories, 10 were involved in protein folding, mainly as chaperones, 7 were metabolic and biosynthesis enzymes including proteins for redox regulation or energy pathways, 3 were involved in cytoskeleton organization, and 3 proteins were related to cellular processes, mainly proteolysis pathways. The viral NS proteins identified as differentially expressed proteins in the analysis were not listed.

In order to identify host factors involved in HCV replication, we examined the effects on viral RNA replication of transfection of SGR-N cells with siRNAs against genes encoding nine proteins belonging to diverse classes of biological functions (Table 1). Each siRNA reduced the HCV RNA level to 47 to 76% of the level of the siRNA control (Fig. 1D). None of the siRNAs tested exhibited considerable cytotoxicity against the replicon cells, ruling out overt toxicity as a mechanism for inhibition of viral RNA replication. Among the candidate

TABLE 1. Selected proteins that reproducibly increased in the DRM fraction of SGR-N cells[a]

Avg ratio	*P* (Student *t* test)	Coverage (%)	Protein name	Molecular function	GI no.
5.56	0.04	27	GRP94	Protein folding	15010550
4.99	0.07	47	Hsp60	Protein folding	6996447
3.73	0.07	6	tRNA guanine transglycosylase	Metabolism	30583205
3.56	0.06	23	KIAA0088	Unknown	577295
3.32	0.07	4	Thioredoxin-related protein	Unknown	20067392
3.32	0.13	12	Tat binding protein 1 (TBP-1)	Cellular processes	20532406
3.06	0.14	22	Aldehyde dehydrogenase 1	Metabolism	2183299
3.06	0.14	14	Chaperonin TRiC/CCT, subunit 2	Protein folding	54696794
2.96	0.04	14	Heat shock 70-kDa protein 4 (HSPA4)	Protein folding	6226869
2.96	0.04	29	GRP58	Metabolism/protein folding	2245365
2.94	0.01	37	Mutant β-actin	Cytoskeleton organization	28336
2.65	0.17	33	Glutathione S-transferase (GST)	Catalytic activity	2204207
2.53	0.04	37	Keratin 19	Cytoskeleton organization	6729681
2.46	0.08	6	Heterogeneous nuclear ribonucleoprotein K	Nucleic acid modification	460789
2.45	0.001	13	HMG-coenzyme A synthase	Metabolism	30009
2.4	0.02	31	CKB	Energy pathway/metabolism	180570
2.4	0.02	11	Cathepsin D	Cellular processes	30582659
2.4	0.02	11	C8orf2	Unknown	37181322
2.36	0.1	38	Tropomyosin 4-anaplastic lymphoma kinase fusion protein	Cytoskeleton organization	14010354
2.36	0.1	6	Calreticulin	Protein folding	30583735
2.33	0.01	29	Quinolinate phosphoribosyltransferase	Metabolism	30583301
2.29	0.04	25	Protein disulfide isomerase-related protein 5	Protein folding	1710248
2.29	0.04	16	Tat binding protein 7 (TBP-7)	Cellular processes	263099
2.05	0.11	24	Calumenin	Metabolism	2809324
2.05	0.12	10	TRiC/CCT, subunit 5	Protein folding	24307939
2.03	0.07	20	Hsp90 beta	Protein folding	34304590
2.01	0.07	10	TRiC/CCT, subunit 1	Protein folding	36796

[a] The spectra obtained by tandem mass spectrometry were collected using data-dependent mode, and the results were subjected to database (NCBInr) search by Mascot server software (Matrix Science, London, United Kingdom) for peptide assignment. Coverage, the ratio of the portion of protein sequence covered by matched peptides to the whole protein sequence. GI no., GenInfo identifier number.

genes examined, we observed a reproducible inhibition of HCV RNA replication by two independent siRNAs targeting CKB (see below).

CKB participates in HCV RNA replication and the propagation of infectious virus. CKB is a brain-type creatine kinase isoenzyme and is also detected in a variety of other tissues, including human liver (32). Steady-state levels of CKB in the DRM fraction, as well as in whole-cell lysate of SGR-N cells were compared to those from parental cells by Western blotting. The CKB level in the DRM fraction of replicon cells was higher than that in parental cells (Fig. 1E), confirming the results of the proteome analysis described above. In contrast, the CKB level in whole cells was similar in both cells (Fig. 1E). These results suggest participation of posttranslational modification, such as translocation to the DRM fraction, of CKB in replicon cells.

Figure 2A shows the inhibitory effect on HCV RNA replication of CKB siRNA; siCKB-2, the sequence of which does not overlap with the sequence of siCKB-1 used in the above siRNA screening (Fig. 1D). Transfection with siCKB-2 effectively decreased the cellular level of CKB enzymatic activity (data not shown), as well as the abundance of CKB protein (Fig. 2A), and resulted in 60% reduction in the viral RNA level in SGR-N cells compared to the cells treated with control siRNA. This inhibitory effect of siRNA on HCV RNA abundance was also observed in JFH-1-derived subgenomic replicon (SGR-JFH1) cells. The viral RNA level in the cells transfected with siCKB-2 decreased by 50% compared to the control (Fig. 2A). We also tested the CKB mutant, CKB-C283S, in which Cys at aa 283, near the catalytic site, has been replaced with Ser (Fig. 3A) and which is known to be enzymatically inactive and to work in a dominant-negative manner (22, 29). As expected, overexpression of CKB-C283S resulted in a reduction in HCV RNA replication in SGR-N cells (Fig. 2B). We obtained a similar result in SGR-JFH1 cells, as described below (Fig. 3E).

To further examine the involvement of CKB in HCV RNA replication, we tested the effect of Ccr, a substrate analogue and possible inhibitor for CK in either SGR-N, SGR-JFH1 (Fig. 2C), or Huh7 cells transiently replicating luciferase-subgenomic replicon (data not shown). We found dose-dependent inhibition of HCV RNA replication but no observed effect on total cellular levels of protein and ATP (Fig. 2D) in the replicon setting used.

We next examined whether the knockdown of CKB or treatment with Ccr would abrogate the production of HCVcc. At 72 h posttransfection with siCKB-2, the HCV core level in cells infected with HCVcc was significantly reduced (Fig. 2E). Treatment of the infected cells with Ccr at various concentrations also reduced the intracellular and supernatant core level and subsequently decreased HCVcc production (Fig. 2F). These results demonstrate that suppression of the HCV RNA replication by the siRNA-mediated knockdown of CKB or treatment with CKB inhibitor leads to reduction of the production of infectious virus.

CKB interacts with HCV NS4A. Having established a role for CKB in HCV RNA replication, we then tried to determine to how CKB influences the HCV life cycle. It has been re-

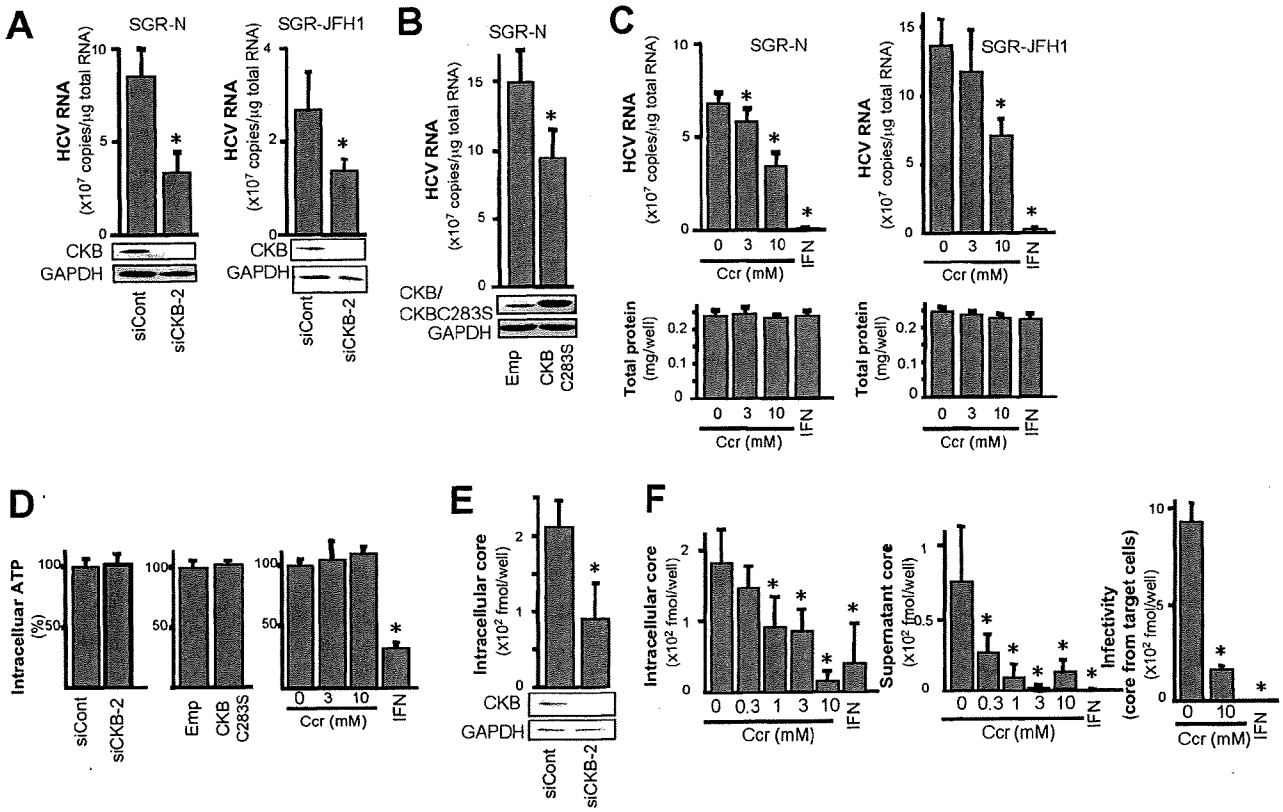

FIG. 2. Involvement of CKB in HCV replication. (A and E) Knockdown of endogenous CKB in SGR-N and SGR-JFH1 cells (A) or HCVcc-infected cells (E). Cells were transfected with siRNA against CKB (siCKB-2) or control siRNA (siCont) and were harvested at 72 h posttransfection. Real-time RT-PCR for HCV RNA levels and immunoblotting for CKB and GAPDH were performed. (B) SGR-N cells were transfected with pCAGCKB-C283S or empty vector, and HCV RNA levels and expression of CKB and CKB-C283S were determined 72 h posttransfection. SGR-N and SGR-JFH1 cells (C) or HCVcc-infected cells (F) were treated with Ccr at various concentrations for 72 h, followed by quantification of HCV RNAs and total cellular proteins. ATP levels (D) were determined after transfection with siCKB-2, pCAGCKB-C283S, or treatment with Ccr for 72 h in SGR-N cells. The ATP levels in the cells transfected with negative control siRNA (left), empty vector (middle), and no treatment (right) were set at 100%, respectively. (F) HCVcc-infected cells were treated with Ccr, and the viral core protein levels in cells (left) and supernatants (middle) were determined at 72 h postinfection. Collected culture supernatants were inoculated into naive Huh-7.5.1 cells after the removal of Ccr. After 72 h, the core proteins in cells were determined (right panel). All data are presented as averages and standard deviation values for at least triplicate samples. *, $P < 0.05$ against control such as transfection with siCont (A and E) or empty vector (B) or nontreatment (C, D, and F).

ported that interaction of CKB with some cellular proteins is required for local availability of CKB activity and local generation of ATP (22, 29). To examine the possible interaction of CKB with HCV NS proteins, HA-tagged CKB (HA-CKB) was coexpressed with FLAG-tagged NS proteins (NIHJ1 strain), followed by immunoprecipitation with an anti-FLAG antibody. CKB was shown to specifically interact with NS4A. No or little interaction was observed between CKB and either NS3, NS4B, NS5A, or NS5B (Fig. 3B). CKB-NS4A interaction was also found with the JFH-1 strain (Fig. 3C).

To identify the CKB region required for the interaction with NS4A, various deletion mutants of CKB were generated (Fig. 3A). An immunoprecipitation assay indicated that NS4A was coimmunoprecipitated with either a full-length CKB, a C-terminal deletion (aa 1 to 357), an N-terminal deletion (aa 297 to 381), or CKB-C283S, but not with aa 1 to 296, aa 1 to 247, or aa 1 to 184 (Fig. 3D, upper middle panel). Further, internal deletions of CKB (CKBdel297-357 and CKB-C283Sdel297-357) failed to interact with NS4A (Fig. 3D, lower panel), suggesting that aa 297 to 357 of CKB are important for its interaction with NS4A. It is noted that the expression of CKB aa 297 to 357 in cells was undetected, presumably due to its misfolding and/or instability. To verify a role for CKB-NS4A interaction in HCV RNA replication, we further determined the effect of expression of either CKB-C283S or its internal deletion lacking aa 297 to 357 (CKB-C283Sdel297-357) on viral replication in SGR-JFH1 cells. As expected, the HCV RNA level was significantly decreased by CKB-C283S, whereas this effect was not observed by CKB-C283Sdel297-357 (Fig. 3E).

NS4A is a 54-residue small protein composed of three domains: the N-terminal membrane anchor, the central domain responsible for interacting with NS3, and the C-terminal acidic domain. To define the portion in NS4A responsible for its interaction with CKB, we constructed three NS4A deletion mutants, each separately expressing one of the NS4A domains, with a FLAG tag (Fig. 3F). CKB proved to interact with the central domain, aa 21 to 39, of NS4A, which is involved in

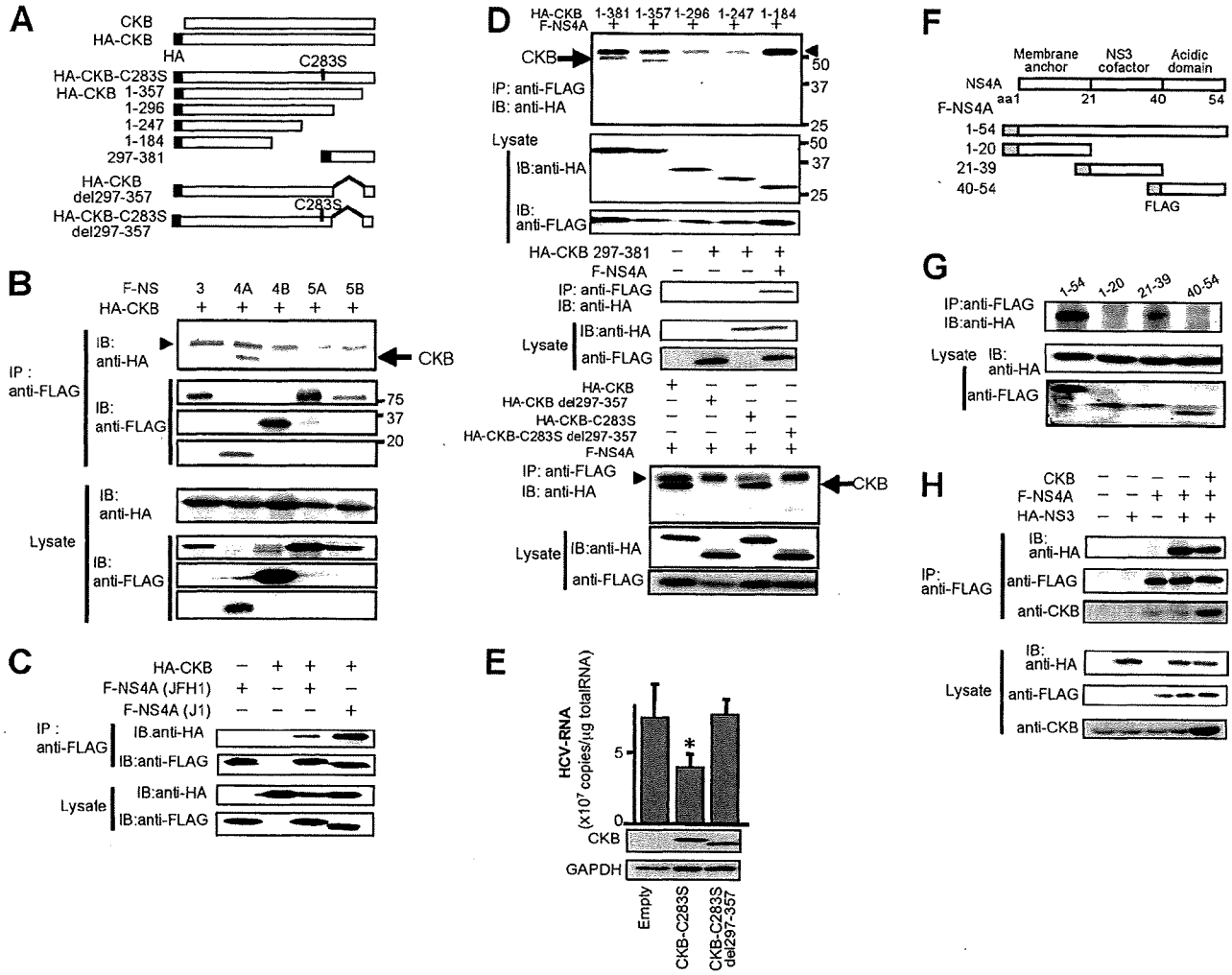

FIG. 3. CKB interacts with HCV NS4A. (A) Structures of CKB constructs used in the present study. A full-length wild-type CKB without an epitope tag (CKB) or with an N-terminal HA tag (HA-CKB), HA-CKB with deletions (aa 1 to 357, aa 1 to 296, aa 1 to 247, aa 1 to 184, and aa 297 to 381 and del297-357), CKB mutant at the catalytic site, Cys-283 (CKB-C283S) or CKB-C283S lacking aa 297 to 357 (CKB-C283Sdel297-357) are shown. HA-CKB was coexpressed with FLAG-tagged versions of each NS protein of strain NIHJ1 (B) or with NS4A of strain JFH-1 (C) in 293T cells and immunoprecipitated (IP) with an anti-FLAG antibody. Immunoprecipitates were subjected to immunoblotting (IB) with anti-HA or anti-FLAG antibody. (D) Each CKB deletion mutant was coexpressed with FLAG-NS4A in 293T cells. Immunoprecipitates were analyzed by immunoblotting. Arrow, CKB; arrowhead, immunoglobulin heavy chain. (E) SGR-JFH1 cells were transfected with the expression plasmid for CKB-C283S, CKB-C283Sdel297-357 or empty vector. At 72 h posttransfection, HCV RNA levels and the expression of CKB and CKB-C283S were determined by real-time RT-PCR and immunoblotting with anti-HA antibody, respectively. For HCV RNA quantitation, data are indicated as averages and standard deviations ($n = 3$). *, $P < 0.05$ against the empty vector control. (F) Structure of NS4A and NS4A constructs. FLAG-tagged NS4A (aa 1 to 54) or its truncated mutants (aa 1 to 20, aa 21 to 39, or aa 40 to 54) are shown. (G) Each NS4A deletion mutant was coexpressed with HA-CKB and analyzed as described above. (H) FLAG-NS4A was coexpressed with HA-NS3 or HA-NS3 and CKB, followed by immunoprecipitation with anti-FLAG antibody. Immunoprecipitates were analyzed by immunoblotting with anti-HA, anti-FLAG or anti-CKB antibody.

formation of the NS3-NS4A complex (Fig. 3G). We therefore investigate whether NS3-NS4A interaction is affected in the presence of CKB and found that exogenous expression of CKB has no influence on NS3-NS4A interaction, and a putative NS3-NS4A-CKB complex was detected in the coimmunoprecipitation analysis (Fig. 3H). Collectively, these results strongly suggest that CKB plays a key role in HCV RNA replication via interaction with NS4A.

Subcellular localization of CKB and NS4A in cells replicating HCV RNA. CKB is distributed throughout cells but is mainly localized in the perinuclear area (31), whereas NS4A is predominantly localized at the endoplasmic reticulum and mitochondrial membranes (37). We examined the possible subcellular colocalization of CKB and NS4A in SGR-N cells by immunofluorescence staining (Fig. 4A). CKB tended to gather in the perinuclear area of HCV replicating cells and was partially colocalized with NS4A in the area, sharing a dotlike structure. To further analyze the subcellular compartments in which CKB and NS4A coexist, we used double-labeling immunoelectron microscopy on SGR-N cells using antibodies against CKB and NS4A, with secondary antibodies coupled to 12- and 18-nm gold particles, respectively. One fraction of

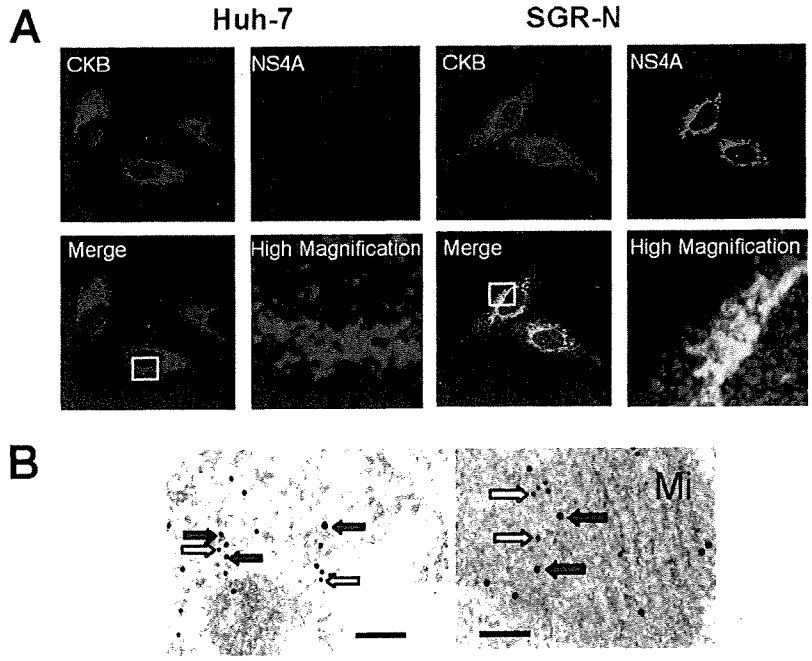

FIG. 4. Colocalization of CKB with HCV NS4A. (A) Indirect immunofluorescence analysis. The primary antibodies used were anti-CKB goat PAb (red) and anti-NS4A MAb (green). Merged images of red and green signals are shown. High-magnification panels are enlarged images of white squares in the merge panels. (B) Immunoelectron microscopic localization of CKB and NS4A. SGR-N cells were double-immunolabeled for CKB (12-nm gold particles; white arrows) and for NS4A (18-nm gold particle; gray arrows). Mi, mitochondria. Bars, 200 nm.

CKB colocalized with NS4A in the cytoplasmic electron-dense regions, presumably derived from altered or folded membrane structures (Fig. 4B, left panel) and mitochondria (Fig. 4B, right panel).

CKB enhances functional HCV replicase and NS3-4A helicase. NS4A is known to mediate membrane association of the NS3-4A complex and to function as a cofactor in NS3 enzyme activity. To understand the mechanism(s) underlying positive regulation of HCV RNA replication through CKB via its interaction with NS4A, we first investigated whether CKB modulates NS3-4A helicase activity. NS3-4A helicase is a member of the superfamily-2 DexH/D-box helicase, which unwinds RNA-RNA substrates in a 3′-to-5′ direction. During RNA replication, the NS3-4A helicase is believed to translocate along the nucleic acid substrate by changing its protein conformation, utilizing the energy of ATP hydrolysis (9). We then tested the effect of CKB on RNA- or DNA-unwinding activity using purified recombinant full-length NS3 and NS3-4A complex (12). As shown in Fig. 5A (left middle panel), both NS3 and NS3-4A helicase activity unwound dsRNA substrate most efficiently when CKB, ATP, and pCr were added to the reaction mixture. The enhancing effect of CKB was observed in the presence of pCr but not in the absence of it, suggesting that catalytic activity of CKB is important for its effect on the HCV helicase activity. Similar results were obtained from the DNA helicase assay using dsDNA substrate (Fig. 5B). To address the specificity of the stimulation by the CKB/pCr system, effects of PK and pPy, which are also involved in the ATP generation, were determined (Fig. 5A, right panels). Exogenous PK and pPy at the same concentrations as those of CKB and pCr used in the study exhibited no effect on the HCV helicase activity.

The effect of CKB on NS3-4A serine protease activity, which is considered to be ATP-independent, was also assessed in an in vitro protease assay using the purified viral proteins as mentioned above (Fig. 5C). As expected, NS3-4A complex exhibited significantly higher activity than NS3 alone; however, CKB did not affect the protease activities of NS3 or NS3-4A.

Finally, we investigated loss and gain of function of CKB in HCV replicase activity, which requires high-energy phosphate, in the context of semi-intact replicon cells. Miyanari et al. (33) reported that the function of the active HCV RC can be monitored in permeabilized replicon cells treated with digitonin. Thus, permeabilized replicon cells in the presence or absence of exogenous CKB were incubated with [α-^{32}P]UTP to detect newly synthesized RNA. As indicated in Fig. 5D, an ~8-kb band corresponding to HCV subgenomic RNA was most abundant in cells in the presence of exogenous CKB, ATP and pCr. The enhancing effect of CKB was observed in the presence but not in the absence of pCr, suggesting that catalytic activity of CKB is important for its effect on the replicase activity. As for the RNA helicase assay, exogenous PK and pPy did not enhance the replicase activity (data not shown). HCV replicase activity in permeabilized cells to which we had introduced siCKB-2 was diminished compared to that in siRNA control-treated cells. Interestingly, the replicase activity in the CKB-depleted cells was recovered by the addition of CKB. Thus, our findings suggest that CKB functions as a key regulator of HCV genome replication by controlling energy-dependent viral enzyme activities.